Appl. Phys. B 75, 469–487 (2002)
DOI: 10.1007/s003400200861

Applied Physics B
Lasers and Optics

Invited paper

J. REICHEL

Microchip traps and Bose–Einstein condensation

Max-Planck-Institut für Quantenoptik und Sektion Physik der Ludwig-Maximilians-Universität,
Schellingstr. 4, 80799 München, Germany

Received: 28 March 2002
Published online: 14 May 2002 •

ABSTRACT The article gives an overview of the rapidly evolving field of magnetic microchip traps (also called 'atom chips') for neutral atoms. Special attention is given to Bose–Einstein condensation in such traps, to the particular properties of microchip trap potentials, and to practical considerations in their design. Scaling laws are developed, which lead to an estimate of the ultimate confinement that chip traps can provide. Future applications such as integrated atom interferometers are discussed.

PACS 03.75.Fi; 32.80.Pj; 39.25.+k

1 Introduction

The achievement of Bose–Einstein condensation (BEC) in a gas of neutral atoms [1–3] brought the quantum and everyday worlds closer together than they ever were. For example, manifestations of superfluidity, such as vortices and vortex lattices [4–6], can be imaged in momentum space; interfering matter-wave functions can now be looked at with a simple video camera [7, 8], etc. Some important consequences of this development appear very clearly in the 'atom laser' [9–12]: its concept underlines the deep analogy of light and matter and, at the same time, the term suggests the possibility of new and far-reaching applications. However, standard BEC experiments still impose formidable technical challenges, which restrict their use to a few dozen advanced laboratories and limit the complexity of atom laser experiments to very elementary configurations. Two recent experiments [13, 14] have demonstrated that an alternative way to BEC exists, which simplifies the apparatus in a dramatic way. In these experiments, microscopic lithographic conductors on a chip replace the customary magnetic coils that are used to confine the atoms in standard BEC experiments. Such a lithographic 'chip trap', first demonstrated three years ago [15], significantly simplifies the trap setup, because modest electric currents can produce large magnetic field gradients and curvatures in close proximity to a planar arrangement of wires [16]. The strong confinement of chip traps also accelerates the condensation process – by more than a factor of 10 [13] compared to typical experiments, and by a factor of three with respect to the all-optical BEC reported recently [17]. This, in turn, entails great simplifications in the vacuum system. As a result, BEC can now be obtained with a setup that is only slightly more complicated than that of a vapor-cell magneto-optical trap (MOT), which is routinely used as a tool in many areas of physics, and is simple enough even for undergraduate laboratories.

In contrast to traditional BEC experiments, the chip trap produces a condensate in close proximity to a room-temperature surface. To date, the interactions of the trapped atoms with the surface have only been studied theoretically [18–20]. The high degree of control over the atomic position in a chip trap may enable surface studies of a new kind. At the same time, it seems clear that surface effects will also impose the ultimate limits to the trap–surface distance. For certain applications, the usefulness of chip traps will depend on how well the surface-induced losses, heating, and decoherence can be controlled; this is especially true for applications that require potentials to vary on submicron length scales. However, even at relatively large distances where surface effects are negligible, on-chip microconductors can generate confining potentials with exquisite properties. These include traps with extremely strong confinement and correspondingly small ground-state size, strongly anisotropic traps with extreme aspect ratio, fundamental systems such as double wells with adjustable barrier height, and devices such as beam splitters or ring resonators. Most intriguingly, however, lithographic fabrication techniques make it possible to integrate even complex systems of many microscopic traps, waveguides [21, 22], and other atom optical devices [23–25] on a single trapping chip. The combination of these advantages – simplicity, modularity, miniaturization, and also robustness – makes the chip trap technique attractive for a wide range of situations, including fundamental studies of condensates with fluctuating phase and in reduced dimensionality [26–29], cavity quantum electrodynamics [30–32] with trapped atoms, and applications like atom interferometry [33] and quantum information processing [34, 35].

This article is intended as a practical introduction to the lively subject of chip traps, with special emphasis on three-dimensional traps and Bose–Einstein condensation. To keep its length within reasonable bounds, the scope has been

✉ Fax: +49-89/285-192,
E-mail: jakob.reichel@physik.uni-muenchen.de

limited to three- and two-dimensional confinement ('traps' and 'guides') using microfabricated conductors on planar substrates ('chips'). Thus, experiments with current-carrying discrete wires such as [36–39], with microfabricated electromagnetic or permanent-magnetic mirrors [40–42], and other innovative experiments with planar techniques, such as atom transport with magnetic structures written on videotape [43], all had to be left out. Some subjects that were only scarcely discussed in previous articles are treated in more detail; thus, there are sections on scaling laws and ultimate confinement, and on adiabatic splitting and merging of trapped clouds, for example. On the other hand, only a short overview is given of the results that are available in the literature, and the choice of the emphasized points has of course some personal accents. Where examples are given, they are mostly taken from the Munich experiments, but complete references are given to relevant results of three-dimensional chip trap experiments, as well as chip-based guiding experiments. Thus, while the article does not attempt do give an exhaustive review, together with the cited references it should provide a fairly complete overview, as of early 2002, of the rapidly advancing topic of chip trap experiments and their applications.

2 Magnetic potentials from planar current distributions

2.1 *Magnetic traps for neutral atoms* [44]

The interaction energy of a neutral atom in a magnetic field is generally much weaker than the atom's thermal energy at room temperature, even in the many-Tesla fields of superconducting magnets. Therefore, atoms have to be cooled before they can be magnetically trapped. It is worth noting that neutrons were magnetically trapped before neutral atoms, despite their thousand-times-smaller magnetic moment [45].

Magnetic trapping of neutral atoms was first accomplished in 1985 [46]. Shortly afterwards, orders of magnitude improvements in density and number of trapped atoms were achieved using superconducting traps and different loading schemes [47–49]. Since then, researchers have continued to develop novel magnetic traps, thereby enabling new physics to be explored. Most notably, Bose–Einstein condensation of atomic gases [1–3] was made possible by the development of stable, tightly confining traps. Integrated microtraps, which are the subject of this article, carry on and extend this development.

Magnetic forces are comparatively strong for atoms with an unpaired electron, such as alkalis, resulting in magnetic moments μ_m of the order of the Bohr magneton μ_B. The interaction of a magnetic dipole with an external magnetic field is given by

$$V(\boldsymbol{r}) = -\boldsymbol{\mu}_\mathrm{m}\boldsymbol{B}(\boldsymbol{r}) = -\mu_\mathrm{m}B(\boldsymbol{r})\cos\theta\,. \tag{1}$$

Classically, the angle θ between the magnetic moment and the magnetic field is constant due to the rapid precession of $\boldsymbol{\mu}_\mathrm{m}$ about the magnetic field axis. Quantum-mechanically, the energy levels of a particle with angular momentum F and g-factor g in a magnetic field are $E(m_F) = g\mu_\mathrm{B}m_F B$, where m_F is the quantum number of the component of F along the direction of $\boldsymbol{B}$. The classical term $\cos\theta$ is now replaced by m_F/F; the classical picture of constant θ is equivalent to the system remaining in a state with fixed m_F.

Depending on the sign of gm_F, the particle experiences a magnetic force either towards minima of the field ($gm_F > 0$, weak-field-seeking state) or towards maxima ($gm_F < 0$, strong-field-seeking state). As Maxwell's equations do not allow a maximum of the magnetic field in free space [50, 51], only weak-field seekers can be trapped. In atomic physics experiments, such states are usually prepared by optical pumping. It is worth noting that the trapped state, being a low-field seeker, is not the state of lowest energy in the presence of the trapping field.

2.1.1 Stability against spin-flip losses. Because magnetic traps only confine weak-field-seeking states, atoms will be lost from the trap if they make a transition to a strong-field-seeking state. Such transitions can be induced by the motion in the trap, because the atom sees a field which is changing in amplitude and direction. The trap is stable only if the atom's magnetic moment adiabatically follows the direction of $\boldsymbol{B}$. This requires that the rate of change of the field's direction θ (in the reference frame of the moving atom) must be slower than the precession of the magnetic moment:

$$\frac{\mathrm{d}\theta}{\mathrm{d}t} < \frac{\mu_\mathrm{m}|\boldsymbol{B}|}{\hbar} = \omega_\mathrm{Larmor}. \tag{2}$$

The upper bound for $\mathrm{d}\theta/\mathrm{d}t$ in a magnetic trap is the trapping frequency. This adiabaticity condition is violated in regions of very small magnetic field, creating regions of trap loss due to 'Majorana transitions' into untrapped states[1] [52].

2.1.2 Quadrupole-type traps. Static magnetic traps can be subdivided into two classes: those in which the minimum is a zero crossing of the magnetic field, and those which have a minimum around a finite field value [53]. In the first case, the potential near the minimum can usually be approximated by a linear function, characterized by its gradient: $\boldsymbol{B} = B'_x x\boldsymbol{e}_x + B'_y y\boldsymbol{e}_y + B'_z z\boldsymbol{e}_z$. Maxwell's equations require $B'_x + B'_y + B'_z = 0$. In macroscopic traps, this configuration is usually realized with two coils in 'anti-Helmholtz' configuration. This is the configuration that was first used to trap neutral atoms magnetically [46].

When quadrupole traps were employed for the first demonstrations of evaporative cooling with alkali atoms [54, 55], trap loss due to Majorana transitions [46, 52, 56] near the zero of the magnetic field was encountered. For atoms moving at a velocity v, the effective size of this 'hole' in the trap is $\sqrt{2\hbar v/\pi\mu_\mathrm{m}B'}$, which is about 1 μm for $\mu_\mathrm{m} = \mu_\mathrm{B}$, $v = 1$ m/s, and $B' = 10$ T/m. As long as the hole is small compared to the cloud diameter, the trapping time can be long (even longer than a minute), and evaporative cooling in such a trap was used to increase the phase-space density by more than two orders of magnitude [57]. As the temperature drops, however, the trap loss due to the hole becomes prohibitive for further cooling. Although the size of the hole shrinks with the thermal velocity of the atoms, the diameter of the atom cloud

[1] In other words, during such a transition, the magnetic field turns, but the atomic spin does not. Considering this, the expression 'spin-flip transition' is somewhat misleading.

shrinks even faster, resulting in a T^{-2} dependence of the loss rate [57, 58].

2.1.3 Ioffe–Pritchard traps. The lowest-order (and therefore tightest) trap which can have a nonzero field in the minimum is a harmonic trap. Indeed, in a linear (quadrupole) trap, the effect of a bias field is merely to displace the zero crossing. A harmonic trap with a bias field $B_{0\|}$ along the x direction has an axial field of $B_x = B_{0\|} + B''x^2/2$. The leading term of the transverse field component B_z is linear, $B_z = B'z$. Applying Maxwell's equations, and assuming axial symmetry, leads to the following field configuration [53]:

$$\boldsymbol{B} = B_{0\|}\begin{pmatrix}1\\0\\0\end{pmatrix} + B'\begin{pmatrix}0\\-y\\z\end{pmatrix} + \frac{B''}{2}\begin{pmatrix}x^2 - \frac{1}{2}\left(y^2+z^2\right)\\-xy\\-xz\end{pmatrix}.$$

The parabolic trap was first suggested and demonstrated for atom trapping by Pritchard [47, 59], and is similar to the Ioffe configuration discussed several decades earlier for plasma confinement [60]. It has become customary to refer to any trap of this field configuration as an Ioffe–Pritchard (IP) trap.

2.1.4 Some general properties of magnetic traps.

Trap depth. A trap of finite depth containing a thermal atomic ensemble (temperature T) will have losses due to atoms 'boiling out of the trap'. As a rule of thumb, the trap depth should be large compared to the mean atomic energy. Neglecting gravity, this leads to the condition

$$V_{\max} = |\mu_{\mathrm{m}} B_{\max}| > \eta k_{\mathrm{B}} T, \tag{3}$$

with $\eta = 5$–7 in order to make this loss term negligible.

Compensation of gravity. For the restoring force $F \propto B'$ along the vertical axis, the minimum requirement is to compensate gravity: $B'_z \geq mg/\mu_{\mathrm{m}}$. Taking the $|F = 2, m = 2\rangle$ state of ^{87}Rb as an example, the minimum field gradient is 0.15 T/m.

Oscillation frequency and ground-state size in a harmonic trap. The oscillation frequency along the ith eigenaxis of a harmonic potential V is given by

$$\omega_i = \sqrt{\frac{1}{m}\frac{\mathrm{d}^2 V}{\mathrm{d}x_i^2}} = \sqrt{\frac{\mu_{\mathrm{m}}}{m}\frac{\mathrm{d}^2 B}{\mathrm{d}x_i^2}}. \tag{4}$$

For ^{87}Rb, $|F = 2, m = 2\rangle$, the frequency $\nu_i = \omega_i/2\pi$ is conveniently calculated as

$$\nu_i = 12.7\ \mathrm{Hz} \times \sqrt{\frac{\mathrm{d}^2 B}{\mathrm{d}x_i^2} / \frac{\mathrm{T}}{\mathrm{m}^2}}.$$

The ground-state extension (1/e radius of $|\Psi|^2$) is given by

$$\delta x_i = \sqrt{\frac{\hbar}{m\omega_i}} = \left(\frac{m\mu_{\mathrm{m}}}{\hbar^2}\frac{\mathrm{d}^2 B}{\mathrm{d}x_i^2}\right)^{-\frac{1}{4}}. \tag{5}$$

For our example state, an oscillation frequency of $\nu = 1$ kHz corresponds to a ground-state extension $\delta x = 340$ nm. To reduce δx by a factor α, B'' must increase by α^4, and therefore very small ground-state sizes become exceedingly difficult to achieve with macroscopic traps. With present-day microtrap technology, on the other hand, it is possible to realize sizes much smaller than an optical wavelength, as will be shown below.

2.2 *Trapping fields from planar current distributions*

When a magnetic potential is created by a system of wires with characteristic size s and carrying a current I, the trapping field gradient and curvature respectively scale as I/s^2 and I/s^3 when s is decreased [16]. Therefore, traps that replace the customary field coils by thin wires on substrates can provide very tightly confining potentials with much less power dissipation than 'traditional' traps using macroscopic coils. Consequently, much stronger traps become realizable with this technique. This section shows how trapping fields are constructed from the fields of coplanar wires, and discusses some simple configurations.

2.2.1 Thin wires and two-dimensional confinement. The magnetic field modulus, gradient, and curvature at a distance r from an infinitely thin wire carrying a current I are

$$B(r) = \frac{\mu_0}{2\pi}\frac{I}{r}, \tag{6}$$

$$B'(r) = -\frac{\mu_0}{2\pi}\frac{I}{r^2}, \tag{7}$$

$$B''(r) = \frac{\mu_0}{\pi}\frac{I}{r^3}. \tag{8}$$

Obviously, to achieve strongly confining traps, it is advantageous to locate the trap center as close as possible to the wire, and this was one of the main motivations for constructing traps with microscopic wires. The wire field alone does not provide trapping because it does not possess a minimum, but there are many ways to construct trapping potentials either with multiple wires or with a combination of wire fields and uniform external fields. The strong confinement in these traps results from the large values of the wire field gradient (7) and curvature (8). A particularly simple and versatile configuration results when a uniform external field $B_{0\perp}$ is added perpendicular to the wire axis: a line of zero field forms at a distance r_0 from the wire axis (Fig. 1):

$$r_0 = \frac{\mu_0}{2\pi}\frac{I}{B_{0\perp}}.$$

On the transverse axis passing through this line of zero field, the wire and external field have the same direction, so that the external field does not affect the field gradient. The transverse field gradient of the total field at r_0 is therefore

$$B'(r_0) = -\frac{2\pi}{\mu_0}\frac{B_{0\perp}^2}{I}. \tag{9}$$

Thus, the superposition of the wire and external fields creates a two-dimensional quadrupole trap, or atom guide, with

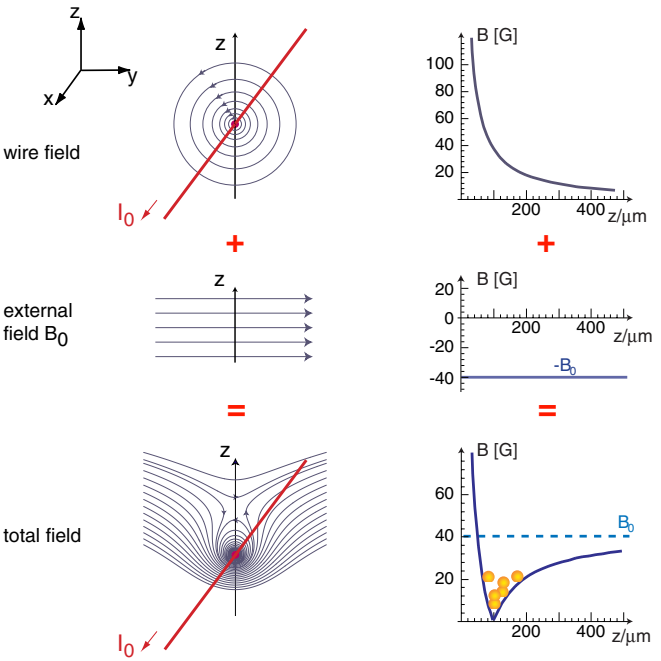

FIGURE 1 Creating a two-dimensional trap with a wire and an external field. *Top*: wire field, *center*: external field, *bottom*: resulting total field. The *left-hand column* shows magnetic field lines and the *right-hand column* gives the magnitude of the field at $y = 0$ for a wire current $I = 2$ A and an external field $B_{0\perp} = 4$ mT. In this example, the trap forms at a distance $r_0 = 100\,\mu$m from the wire axis, and the gradient at the trap center is $|B'(r_0)| = 40$ T/m, assuming an infinitely thin wire

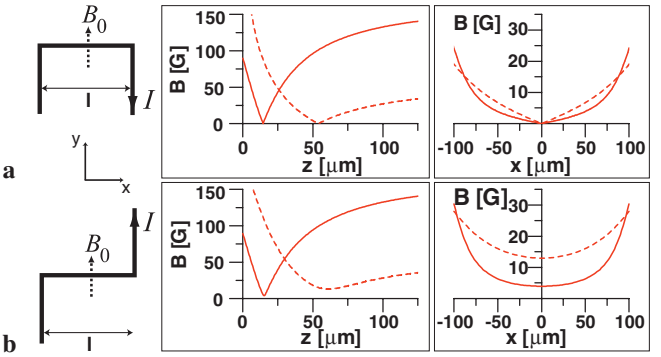

FIGURE 2 Wire layout for a quadrupole (**a**) and an Ioffe–Pritchard trap (**b**), and magnetic potentials generated by these arrangements for $l = 250\,\mu$m and $I = 2$ A. The bias field along y is $B_0 = 5.4$ mT (*dashed lines*) and 16.2 mT (*solid lines*). The potentials shown in the figure were obtained by numerical Biot–Savart-type calculations, taking into account a wire width of 50 μm

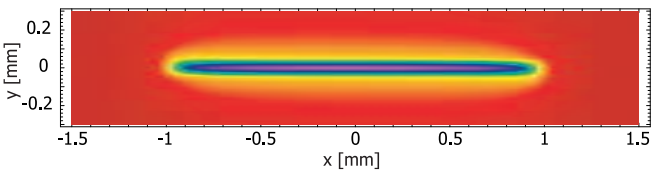

FIGURE 3 Contour plot showing an example of a very elongated magnetic potential generated by a Z-shaped wire (as in Fig. 2b) with $l = 1.95$ mm. The wire carries a current of 2 A and there is a bias field $\boldsymbol{B} = 0.1\,\text{mT}\cdot\boldsymbol{e}_x + 8\,\text{mT}\cdot\boldsymbol{e}_y$. The field is shown in a plane containing the trap center; the distance from the wire plane is $z = 46\,\mu$m. The field of this very elongated trap varies between 0.1 mT in the center and ∼ 8 mT in the corners of the plot

a transverse restoring force proportional to $B'(r_0)$. Arrangements of several parallel wires, either with or without external fields, can also be used to create such guides, and will be discussed below in Sect. 2.2.4.

These simple thin-wire equations are very useful in practice. Of the three parameters I, $B_{0\perp}$, and r_0, two can be chosen independently and the third follows from them. For quick estimates it is convenient to express the equations in the following form:

$$B(r) = 200\,\text{mT} \times \frac{I/\text{A}}{r/\mu\text{m}}, \tag{10}$$

$$B'(r) = -2 \times 10^5\,\text{T m}^{-1} \times \frac{I/\text{A}}{(r/\mu\text{m})^2}, \tag{11}$$

$$r_0 = 200\,\mu\text{m} \times \frac{I/\text{A}}{B_{0\perp}/\text{mT}}, \tag{12}$$

$$B'(r_0) = -5\,\text{T m}^{-1} \frac{(B_{0\perp}/\text{mT})^2}{I/\text{A}}. \tag{13}$$

2.2.2 Three-dimensional wire traps. The two-dimensional trap described in Sect. 2.2.1 can easily be extended to provide confinement along the wire axis as well. For this purpose, the wire is bent at both ends, forming either a 'U' or a 'Z' (Figs. 2 and 3). The central part of the wire (parallel to $\boldsymbol{e}_x$), combined with the external field, produces a two-dimensional quadrupole trap as before. The bent parts of the wire produce a field which is perpendicular to the external field. The x component of this additional field closes the trap along the x axis, while the y component merely causes a small displacement of the minimum. In the 'U' case, the contributions of the two bent parts cancel out in the trap center, leading to a zero field and a linear variation of the field modulus near the trap center. In this sense, the 'U' trap is a quadrupole trap. In the 'Z' case, the two contributions add up instead of canceling out, so that the field in the trap center is now nonzero. This new field contribution is perpendicular to the two-dimensional quadrupole field near r_0, and so the two fields add quadratically: the total field near the trap center is that of an Ioffe–Pritchard trap.

This example shows how the two 'classical' types of magnetic trapping potentials can be generated in a straightforward way with a planar wire and a homogeneous external field. These simple wire traps produce impressively strong confinement, as shown in the example of Fig. 2. By increasing the external field $B_{0\perp}$ while leaving the wire current I unchanged, the trap center moves closer to the wire, into regions of higher field gradient, and transverse confinement becomes stronger. Indeed, in the compressed trap of Fig. 2b, the transverse curvature is 574 MT/m^2, leading to a level spacing (in the harmonic approximation) of 30.4 kHz for ^{87}Rb atoms in the $F = 2, m = 2$ ground state, and to a ground-state size of $\delta x \sim 62$ nm. Note that the potentially critical parameters remain well inside the safe zone for this realistic example: the wire width is 50 μm (much smaller structures have been used for atom trapping), and the distance of the trap center from the surface is ∼ 15 μm. Incidentally, the example shows that it is not necessary to use sophisticated lithographic techniques to obtain trapping in the Lamb–Dicke regime defined by $(\nu_\text{r}/\nu)^2 < 1$, where $\nu_\text{r} = \hbar k^2/(4\pi m)$ is the recoil frequency for absorption or emission of a photon with wave number k.

Depth of a wire trap. In a wire trap with external bias field B_0, the trap depth is simply given by the bias field: $B_{\max} = B_0$, and we have the requirement (cf. (3)) $B_0 > \eta k_B T/\mu_m$, or $B_0 > 1.5\,\mathrm{T/K} \times \eta T$ for $\mu_m = \mu_B$. As an example, for an ensemble of ^{87}Rb atoms in the $|F = 2, m = 2\rangle$ state with a temperature $T = 100\,\mu\mathrm{K}$, the bias field must be at least $B_0 \sim 0.8\,\mathrm{mT}$ (for $\eta = 5$).

2.2.3 Effects of finite wire width. For a cylindrical wire, the field outside the conductor is identical to that of an infinitely thin wire centered on the cylinder axis. Microfabricated wires, however, typically have a rectangular cross section and an aspect ratio smaller than one (width greater than height). The field of a long conductor of this kind is well approximated by that of an infinitely long wire of zero height, but nonzero width w, for which an analytical formula exists [25, 61]:

$$B(z) = \frac{\mu_0}{\pi}\frac{I}{w}\operatorname{arccot}\frac{2z}{w} = \frac{\mu_0}{\pi}\frac{I}{w}\left(\frac{\pi}{2} - \arctan\frac{2z}{w}\right). \qquad (14)$$

Here, z is the distance from the wire surface. A wire of this type will be called a 'broad' wire in this article. For $z \lesssim w$, the formula simplifies to

$$B(z) \approx \frac{\mu_0}{\pi}\frac{I}{w}\left(\frac{\pi}{2} - \frac{2z}{w}\right).$$

In particular, the surface field is

$$B_s = \frac{\mu_0}{2}\frac{I}{w}. \qquad (15)$$

This field constitutes an upper limit to the trap depth that can be achieved with a broad wire. It equals the field created by the same current through an infinitely thin wire at a distance $w/2$. The gradient of the field (14) is

$$B'(z) = -\frac{\mu_0}{2\pi}\frac{I}{z^2 + (w/2)^2}. \qquad (16)$$

Instead of the $1/r^2$ dependence of the thin-wire gradient, the broad-wire gradient is of Lorentzian form. The gradient at the surface is

$$B'_s = -\frac{2\mu_0}{\pi}\frac{I}{w^2}, \qquad (17)$$

which imposes a limit to the achievable trap steepness.

Figure 4 shows the result of a measurement in which (14) was experimentally verified for a conductor with $w = 300\,\mu\mathrm{m}$ and ~ 10-μm height. The deviation from the thin-wire dependence becomes notable for $z \lesssim w$.

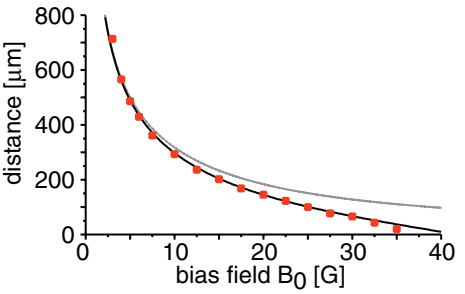

FIGURE 4 Measured distance z between the center of the trapped atom cloud and the surface as a function of the bias-field strength B_0. The trapping field is generated with a 'U'-shaped quadrupole wire as in Fig. 2. The wire width is 300 μm; its current is kept constant at $I = 2\,\mathrm{A}$. *Circles* are experimental values obtained from absorption images, the *solid line* is the calculated position of the potential minimum obtained from (14) for $w = 300\,\mu\mathrm{m}$, and $I = 2\,\mathrm{A}$. For comparison, the *gray line* gives the theoretical position for an infinitely thin wire

2.2.4 Other configurations. Magnetic guides can also be created with many parallel-wire configurations, with and without external fields (Fig. 5); [62] gives a good overview of possible geometries. (That article also discusses the interesting possibility of constructing single-mode guides.) Most of these configurations have been used in guiding experiments, see Sect. 4.2. They can also be used to provide transverse confinement in three-dimensional traps. An example of a three-dimensional trap using the configuration of Fig. 5e is given below in Fig. 16.

2.2.5 Building blocks for complex potentials. The two configurations of Fig. 2 were the first chip traps to be realized experimentally, but there are many more possible trapping configurations, and a wealth of configurations for more complex potentials. A systematic approach to constructing many compound potentials from simple building blocks is presented in [25]; potential design is also discussed in [63]. Two crossing conductors (Fig. 6) form the basis of the systematic approach given in [25]. Such a conductor crossing, used with an appropriate external field, constitutes a particularly simple Ioffe–Pritchard trap as shown in the right-hand column of

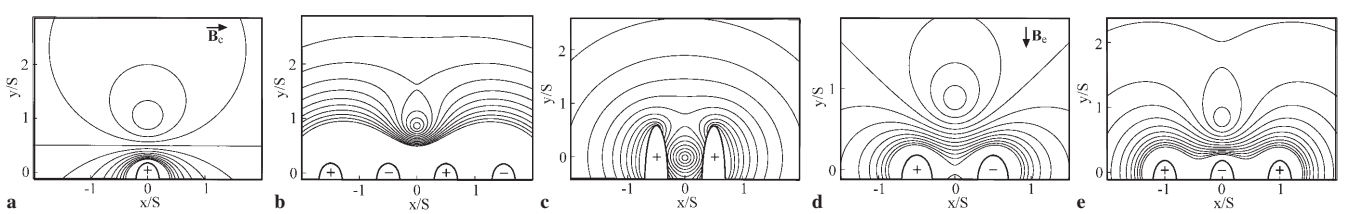

FIGURE 5 Isopotential curves for several magnetic waveguide configurations. The direction of current flow is indicated by '+' and '−'; in-plane external magnetic fields are indicated by *bold arrows*. Twelve contours are shown, equally spaced by $B_0/15$ in **a** and by $B_0/4$ in **b**–**e**, where $B_0 = \mu_0 I/2\pi S$. **a** A single wire with an external field B_e perpendicular to the wire axis; here $S = \mu_0 I/2\pi B_e$. This is the situation of Fig. 1. **b** Four-wire guide; here S is the distance between neighboring wires, and each wire carries a current I. **c** Two high-aspect-ratio wires, separated by S, with co-propagating currents. **d** Two wires, separated by S, with opposing current directions and an external field $B_e = B_0$ in the y direction. **e** Three wires, separated by S, with each outer wire carrying −1.25 times the inner-wire current (adapted from [62])

Fig. 6. As a rule of thumb, the stronger of the two currents provides the transverse confinement, while the weaker one serves to establish the longitudinal minimum. This configuration has been used in an experiment to obtain an IP trap with a rotatable axis orientation. The result is shown in Fig. 7.

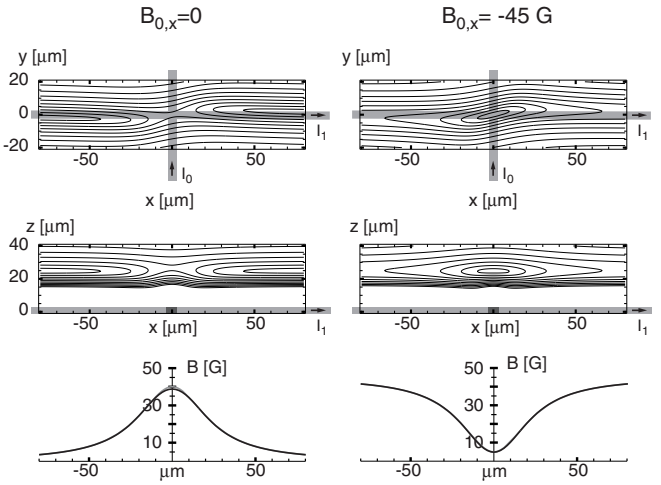

FIGURE 6 Field strength at a wire intersection with parameters $I_0 = 2$ A, $I_1 = 0.5$ A, $B_{0,y} = 160$ G. In the *left-hand column*, no field is applied along $\boldsymbol{e}_x$, and the total field has a 'saddle point', repelling atoms from the conductor intersection. In the *right-hand column*, an additional field $B_{0,x} = -45\,\mathrm{G}\,\boldsymbol{e}_x$ is applied, creating a three-dimensional trap above the intersection point. The *upper* and *middle rows* show contours of the magnetic field modulus (contour-line spacing 10 G). The conductor configuration is indicated by *shaded lines* in the contour plots. The *bottom column* shows the field modulus along the transverse center of the potential

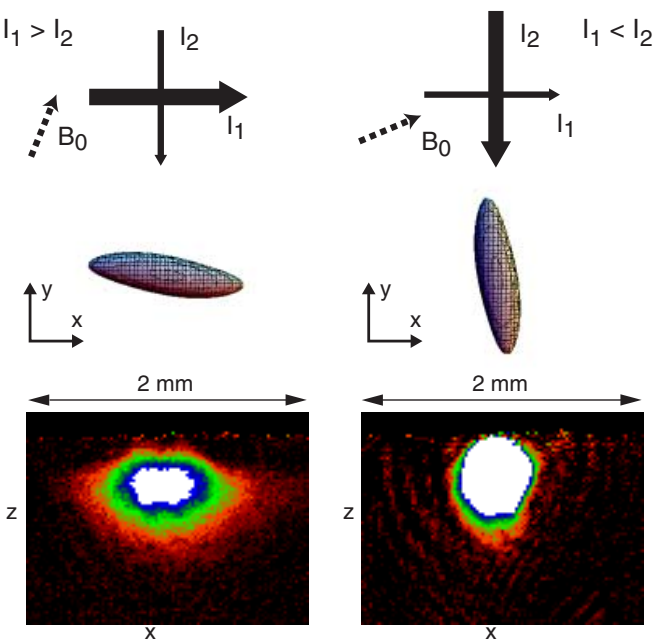

FIGURE 7 Ioffe–Pritchard trap created by two intersecting conductors. The *left-hand column* corresponds to $I_1 > I_2$ and $|B_{0,y}| > |B_{0,x}|$; in the *right-hand column* both relations are reversed. *Top row*: conductor pattern; the thickness of the *arrows* corresponds to the magnitude of the current. *Dashed arrows* indicate the bias-field direction. *Middle row*: calculated contours of the magnetic field modulus $|B(x, y)|$ indicating how the long trap axis turns. The *left-hand potential* continuously transforms into the *right-hand one* when the parameters are changed smoothly. *Bottom row*: absorption images corresponding to the two situations. The final trap (*right*) contains 4.5×10^5 atoms (adapted from [25])

Multiple wire intersections can be combined to obtain more complex potentials. The trapped-atom interferometer potential, shown below in Fig. 12, is an example of this method.

2.2.6 Ultimate confinement: scaling laws and practical limits. Part of the motivation for chip traps comes from the exceptionally strong confinement which they provide. Today's experiments are still far from reaching fundamental limits in this respect, and it is interesting to consider how tight the magnetic confinement can be made. To obtain the strongest possible trap with a given wire, the trap center must be located as close as possible to the wire surface: field gradients are strongest at the wire surface; the thinner the wire, the higher the maximum gradient for a given current. Thus, it might seem at first that the structure-size limit of available microfabrication techniques (e.g. 130 nm in state-of-the-art mass-production processes) would limit the confinement in a chip trap. It turns out, however, that other effects impose much more severe restrictions on the gradient, limited current density being the most important one for small structures. Limitations in the trap–surface distance, which result from interactions of the trapped atoms with the surface, will be discussed in Sect. 6.1. In the present section, the boundary conditions due to the chip alone will be considered.

Practical limits: power and current density. In microelectronics, conventional current-carrying wires are known to fail due to electromigration, which is the thermally assisted motion of ions under the influence of an electric field. For short ($\sim$ 1-μm) gold 'nanowires' of 20-nm height and widths between 60 and 850 nm on silicon substrates, a maximum current density of typically 10^{12} A/m^2 has been measured, which was essentially independent of the wire width [64]. In the context of chip traps, the maximum sustainable current density has been measured by several groups [65]. The thin-film hybrid conductors used in Munich reproducibly sustain current densities of several 10^{10} A/m^2 for a wire cross section of $\sim 10 \times 10\,\mu\mathrm{m}^2$. Although the results scatter considerably, and depend on parameters such as substrate thickness and thermal coupling to the environment, a current density of $j = 10^{11}$ A/m^2 seems to be an upper limit for micron-sized gold conductors at room temperature, and can be increased by roughly an order of magnitude at liquid-nitrogen temperature [65]. Interestingly, superconductors do not offer higher current densities [16]. Nevertheless, they may be useful for long wires to reduce the total power.

The high values of j given above are only reached for relatively thin ($w \lesssim 10\,\mu\mathrm{m}$) wires. Indeed, in a macroscopic gold wire, with a quadratic 0.1×0.1 mm^2 cross section for example, the current density of 11 A/m^2 corresponds to a current of 10^3 A and a dissipated power of 22 kW/cm! When microtraps are scaled to a smaller size, the length-to-width ratio $\beta = l/w$ typically remains constant. The general relationship of w, j, and the total power P can then be expressed as

$$P = \varrho j^2 w^3 \beta, \tag{18}$$

where ϱ is the resistivity, and where we have assumed a quadratic cross section. Even for relatively complex traps, it should be safe to assume $\beta \lesssim 10^3$. (For example, $\beta \sim 750$ in the 'atomic conveyor belt' shown in Fig. 14 below; the thicker conductors which connect to the microscopic wire contribute negligibly to the total power.) If the wire width is reduced at constant j, the total power soon becomes negligible. For a 'safe' total power of 1 W, the turnover from the power-limited to the current-density-limited regime takes place at $w = 357$ nm, a factor 3–10 below the structure size of today's smallest chip traps.

For thicker wires, the total power P may limit the sustainable current before j does. The maximum P is again a value that can vary widely, depending on the choice of materials, the mounting and cooling technique, etc. A power of a few watts can be maintained without active cooling by providing good heat conductivity from the substrate to a metal surface outside the vacuum.

Field gradient. The maximum magnetic field gradient $B'_{\max}$ of a current-carrying straight wire is reached on the wire surface. For a wire with circular cross section and diameter w, its value is $|B'_{\max}| = 2\mu_0/\pi \times I/w^2$. (This is also the gradient at the surface of a 'broad' wire (16).) The current density in this wire is $j = I/\pi(w/2)^2$, and the gradient can be written

$$|B'_{\max}| = \frac{\mu_0}{2} j \,. \tag{19}$$

Obviously, the proportionality of $B'_{\max}$ to j is a general property that is not limited to circular wires, and the prefactor only slightly depends on the shape of the wire cross section.

To increase the gradient $B'_{\max}$, one can either (a) reduce the wire width w at constant current, or (b) increase the current I for a given w. In both cases, both critical parameters are increased: the current density j and the dissipated power P. It depends on the size of the wire which of the two actually limits the gradient (see below); for thin wires, the limitation is due to the limit in j. For $j = 10^{12}\,\mathrm{A/m^2}$, we find $|B'_{\max}| \sim 8 \times 10^5\,\mathrm{T/m} = 8 \times 10^7\,\mathrm{G/cm}$. Reducing the current density by an order of magnitude for safety, and the gradient dependence by a factor of two (corresponding to a realistic trap–surface distance of $w/2$ instead of 0), one still obtains the impressive value of $|B'_{\max}| \sim 4 \times 10^4\,\mathrm{T/m} = 4 \times 10^6\,\mathrm{G/cm}$. For a wire width $w = 1\,\mu\mathrm{m}$, this value would be reached with a total current $I = 0.1$ A and a surface field $B_\mathrm{s} \sim 6 \times 10^{-2}\,\mathrm{T} = 600\,\mathrm{G}$. To check whether the total power remains within realistic limits, we again assume a length-to-width ratio of $\beta = 10^3$: for a gold conductor ($\varrho = 2.2 \times 10^{-8}\,\Omega\,\mathrm{m}$), we find a total power $P = 220\,\mathrm{mW}$, a safe value.

Field curvature and trap frequency. Due to the addition of a bias field (cf. Sect. 2.1.1), stable traps typically have a quadratic potential near the trap center. Taking into account the results of the preceding paragraphs, what is the maximum curvature and trap frequency in a chip trap? For simplicity, we restrict ourselves to the case of a very elongated (i.e. two-dimensional) trap with a transverse field gradient of magnitude B' and a bias field $B_{0\|}$ parallel to the trap axis. Near the trap center, the field is approximated by

$$B(\varrho) = B_{0\|} + \frac{B'^2}{2B_{0\|}}\varrho^2$$

(cf. Sect. 2.1.3), and the transverse frequency (4) is given by

$$\omega = \sqrt{\frac{\mu_\mathrm{m}}{m}\frac{B'^2}{B_{0\|}}}. \tag{20}$$

To obtain a stable trap, $B_{0\|}$ must be chosen in proportion with the trap frequency:

$$B_{0\|} = \alpha\omega \,, \tag{21}$$

with $\alpha \sim 2 \times 10^{-10}\,\mathrm{T\,s}$ to obtain a spin-flip probability of about 10^{-6} per oscillation period [62, 66]. Eliminating $B_{0\|}$ in (20) and assuming a gradient $B' = (\mu_0/4)\,j$ (i.e. half the value at the surface given by (19)) yields

$$\omega = \alpha_j\, j^{\frac{2}{3}} \,, \tag{22}$$

with

$$\alpha_j = \left(\frac{\mu_\mathrm{m}}{\alpha m}\right)^{\frac{1}{3}} \left(\frac{\mu_0}{4}\right)^{\frac{2}{3}} .$$

For $\mu_\mathrm{m} = \mu_\mathrm{B}$ and $m = 1.46 \times 10^{-25}\,\mathrm{kg}$ (mass of ^{87}Rb), the numerical value of this constant is $\alpha_j = 2\pi \times 5.0 \times 10^{-2}\,\mathrm{m^{4/3}\,s^{-1}\,A^{-2/3}}$. The maximum possible oscillation frequency is obtained by inserting the maximum current density into (22). With $j = 10^{11}\,\mathrm{A/m^2}$, the result for our example state is $\omega_{\max} = 2\pi \times 1.1\,\mathrm{MHz}$, with a corresponding ground-state size (5) $\delta x = 10\,\mathrm{nm}$, and results from a gradient $B' = 3.1 \times 10^4\,\mathrm{T/m}$.

In summary, when scaling down the wire dimensions, a regime is reached where the current density must be held constant. As soon as this happens, further reduction of the wire width does not lead to stronger gradients, because the maximum field gradient scales as the current density. The highest reported current densities lie between $10^{11}\,\mathrm{A/m^2}$ (at room temperature) and $10^{12}\,\mathrm{A/m^2}$ (with liquid-nitrogen cooling), leading to maximum gradients in the $10^5\,\mathrm{T/m}$ region.

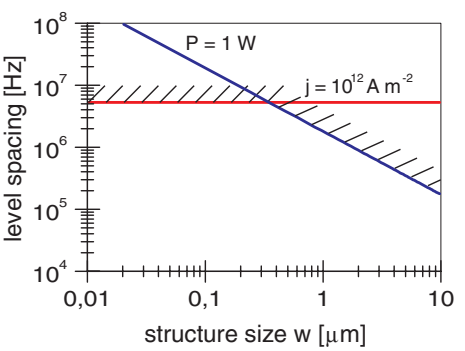

FIGURE 8 Maximum achievable level spacing in a chip trap as a function of the structure size, for the case of the ^{87}Rb, $|F = 2, m = 2\rangle$ state, assuming a maximum current density of $10^{11}\,\mathrm{A\,m^{-2}}$ and a maximum total power of 1 W. *Hatched lines* mark the inaccessible region according to these boundary conditions. The constant-power curve was calculated from (18) (with $\beta = 10^3$) and (22)

Today's strongest traps only reach $\sim 250\,\mathrm{T/m}$, so that there is still a lot of room for improvement. Even in the regime of constant current density, further size reduction may be helpful to obtain potentials with smaller length scales. However, atom–surface interactions (cf. Sect. 6.1) may impose more severe limits than the current density does. For ^{87}Rb, the conclusion is that trapping far into the Lamb–Dicke regime is a realistic goal, whereas a trapping frequency larger than the line width of the cooling transition (i.e. resolved sidebands) will be hard or impossible to reach. Figure 8 summarizes these results.

3 Microfabrication processes for chip traps

A priori, almost all standard microfabrication processes can be used in chip trap experiments. Standard conductor metals such as gold or aluminum, semiconductors such as silicon or gallium arsenide, common ceramic materials such as aluminum oxide or aluminum nitride, and even some photoresists and SMD (surface-mounted device) electronic components possess suitable characteristics: they have fairly low to excellent outgassing rates, can be baked to 120 °C or more, and do not react strongly with alkalis. This means that a wealth of well-established methods and devices is available, which can potentially help atom optics experiments to break fresh ground. The experiments discussed in this article only use microfabricated conductors – they are most elementary devices. Nevertheless, their combination with atomic physics methods has already enabled novel and very promising experiments. The future will show whether more elaborate micro- and nanotechniques can be employed to go still further and realize true 'integrated atom optics' [67, 68].

Current implementations of the chip trap method use relatively large-scale conductors. The thinnest wires that were used in the experiments published to date were 3-μm wide [14]. To maintain high currents in these structures, it is desirable to have a wire height of the same order (i.e. quadratic cross section). The corresponding layer thickness of several micrometers is unusually large for direct lithography techniques. Only the Innsbruck/Heidelberg group has used a purely lithographic process [69]. All other experiments so far have used combinations of lithography and electroplating. A commercial process of this type is thin-film hybrid technology, used routinely in microwave and high-performance electronics. A very similar process is described in [65].

A wide variety of substrate base materials exists, and many of them are used for volume production in electronics and are inexpensive. For example, alumina (Al_2O_3), aluminum nitride (AlN), and sapphire are standard substrate materials in thin-film hybrid technology; passivated Si and GaAs are routinely used in microelectronics. Tables 1 and 2 list properties

Material	Therm. conductivity (at 20 °C) ($\mathrm{W\,m^{-1}\,K^{-1}}$)	Lin. expansion coefficient ($10^{-6}\,\mathrm{K^{-1}}$)	Density ($\mathrm{g\,cm^{-3}}$)	Transmission range (nm)
BeO	260–300	8.4–9.0	2.86	
AlN	170–180	4.4–5.3	3.25	500–3000
Al_2O_3 (sapphire)	35–40	5.8	3.99	200–5500
Al_2O_3 (alumina)	26–35	8.0	3.9	
SiO_2 (fused quartz)	1.46	0.54	2.2	180–2500
BK7	1.11	8	2.51	400–1400
Pyrex	1.13	3.25	2.23	300–2500
Polyimide	0.1–0.35	30–60	1.42	
C (diamond)	200–2000	0.8	3.52	400–300 000
GaAs	∼ 55	6.0	5.3	1500–14 000
Si	80–150	4.7–7.6	2.34	1200–15 000

TABLE 1 Properties of some nonmetallic materials. Of the ceramic materials, BeO has the best heat conductivity, but is rarely used because of its toxicity. Polyimide is a ultrahigh vacuum compatible polymer. It is used in electronics, e.g. as a base material for flexible circuits, and as an insulating layer in multilayer boards. The properties of diamond, gallium arsenide, and silicon strongly depend on the purity

Material	Resistivity ϱ ($10^{-8}\,\Omega\,\mathrm{m}$)	Temp. coeff. of ϱ (0–100 °C) ($\mathrm{K^{-1}}$)	Therm. conductivity (0–100 °C) ($\mathrm{W\,m^{-1}\,K^{-1}}$)	Lin. expansion coefficient ($10^{-6}\,\mathrm{K^{-1}}$)	Density ($\mathrm{g\,cm^{-3}}$)	Melting point (°C)
Ag	1.63	0.0041	429	19.1	10.5	961.9
Cu	1.69	0.0043	401	17.0	8.96	1083
Au	2.20	0.0040	318	14.1	19.30	1064.4
Al	2.67	0.0045	237	23.5	2.70	660.4
Na	4.5	0.0055	128	71	0.97	97.8
In	8.8	0.0052	81.8	24.8	7.3	156.6
Fe	10.1	0.0065	80.4	12.1	7.87	1535
Pt	10.58	0.00392	71.6	9.0	21.45	1772
Rb	12.1	0.0048	58.2	9.0	1.53	38.9
Stainless steel	70–78		16.3	15–18	∼ 7.9	∼ 1400

TABLE 2 Properties of some metals, ordered by resistivity

of nonmetallic and metallic materials, respectively, that are of potential interest for chip trap fabrication.

For use with a mirror MOT (Sect. 4.1.1 below), the chip (or a part of it) must have a reflective surface. One method to achieve this is to metal-coat the whole chip surface with the exception of narrow etchings separating the conductors. This was done in [69], achieving a very good overall reflectivity, but some inevitable diffraction at the etchings. Alternatively, a replica method [25] can be used to transfer a reflective layer onto the chip surface. In this case, a layer of epoxy glue separates the chip/conductor relief from the mirror layer. This epoxy layer fills the gaps between conductors, so that the mirror layer has no edges and is flat. However, application of this method requires some training, and it is difficult to obtain a good overall mirror quality. Mirror quality is not critical for the MOT, but if fluorescence imaging is desired, low scattering from the surface is essential.

4 Chip trap experiments I: thermal atoms

In mid-1998, chip traps were just an interesting idea among many other proposed designs for novel magnetic traps; of those who cared enough to take notice of the concept, many were probably doubtful about its chances of success. One year later, the Munich experiment had shown that rubidium atoms could indeed be trapped as proposed [15]; at about the same time, atom guiding on a chip was demonstrated in Boulder [21] and Cambridge [22]. Soon a second trapping experiment followed suit [69], this time with lithium, set up by a team in Innsbruck (now in Heidelberg), who had long experience with discrete-wire experiments. Many more people now took notice of the concept thanks to the publicity effort of that group, which resulted in numerous articles describing their result and their vision of an 'atom chip'. In the following years, experiments started to use the freedom of lithographic design for demonstrating new magnetic manipulation devices: splitters [23, 24] and a switch [70] for thermal atomic beams, a magnetic 'conveyor belt' [71] for adiabatic transport of trapped thermal clouds, and more exotic devices such as a linear collider for atom clouds [25]. Still, many were doubtful about current noise and surface effects, which might be too severe to support the fragile state of a Bose–Einstein condensate. Meanwhile, a group in Tübingen, having gained wide experience with discrete-wire traps, produced their first lithographic substrate and loaded it with atoms in early 2001. Both the Munich and the Tübingen teams now began to study evaporative cooling in chip traps, and succeeded in obtaining on-chip Bose–Einstein condensates in the beginning of June 2001 [13, 14], with almost perfect synchronicity: June 08 in Tübingen, June 12 in Munich.

The present section discusses the key issue of trap loading, and summarizes the experiments done with thermal atoms in chip traps and guides. A discussion of the on-chip BEC follows in Sect. 5.

4.1 *Chip trap loading*

Trap loading is a crucial issue for chip trap experiments. In experiments with cold atoms – including 'traditional' BEC experiments – the cloud of cooled atoms is usually kept as far away as possible from material surfaces. (Evanescent-wave traps [72] are a notable exception to this rule.) In fact, in 1996 it was known that chip traps would produce very strong traps ideally suited for evaporative cooling [16], but no suitable loading mechanism was available. The first successful chip trap experiment [15] solved the loading problem by introducing the 'mirror-MOT', and employing it in a loading sequence similar to a standard BEC experiment. This approach is now widely employed in surface-trapping experiments (see e.g. [43, 69]), and is outlined in Sect. 4.1.1 below. Alternatively, the atomic cloud can be first stored and eventually precooled in a macroscopic trap, and then transferred into the chip potential by a conservative force, which may be derived from a magnetic [14] or an optical [73] potential. Both methods have specific advantages, as will be discussed in the following sections.

Both of the above methods work in a pulsed mode. For some experiments – especially for interferometers using 'matter waveguides' [74, 75] – continuous loading may be desirable. (Note, however, that integrated atom interferometers are also possible with trapped atoms, as described below in Sect. 6.3.) The main problem for continuous loading, outlined in Sect. 4.1.3, consists in efficient coupling from the cold-atom source into the waveguide.

A more radically different approach would be to use a laser-less source of cold atoms. Some pioneering work has been done in this direction [76, 77]. For the time being, however, such a solution comes at the price of reduced flux of sufficiently cold atoms and additional complications in the experimental setup. It would be interesting to consider whether a laser-less source can be realized on a chip. In view of future 'real-life' applications, a loading solution without lasers has a lot of appeal.

4.1.1 Direct loading from a mirror-MOT. The standard magneto-optical trap setup [78, 79] is the combination of six red-detuned beams along three orthogonal axes with a magnetic quadrupole field (Fig. 9a). The sub-Doppler cooling and trapping mechanisms require a particular choice of beam polarizations: all six beams are circularly polarized; the two beams on the quadrupole axis have equal helicity, which is opposite that of the other four beams. The MOT has proven to be a remarkably robust tool – for example, MOTs have been

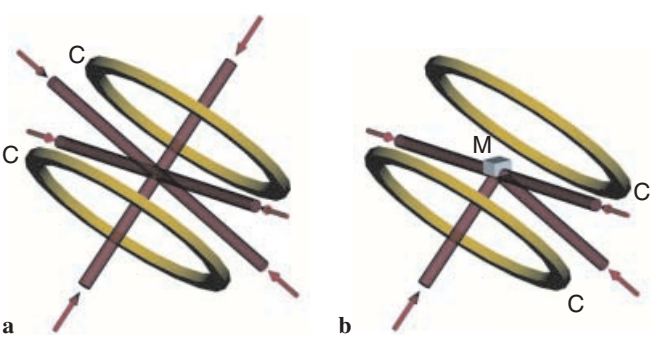

FIGURE 9 **a** Geometry of the standard magneto-optical trap (MOT). C: quadrupole field coils. The helicity of the two beams on the quadrupole axis is equal and opposite to that of the other four beams. **b** Modified scheme to enable trapping near a surface ('mirror-MOT'). M: mirror. The mirror is placed in such a way that the reflected beams have the same helicity as their counterparts in the standard setup

observed to work with divergent beams, with linear instead of circular polarization in one of the beams, with four beams in a tetrahedral configuration [80], and in the harsh environment of an airplane performing parabolic flights [81]. Here, the goal is to modify the setup in such a way that the cloud of cold atoms is located in close proximity to a surface – the trapping chip. The exact value of the required MOT–surface distance is the maximum distance at which the on-chip current can produce a stable magnetic trap, and is typically 1 mm or less.

The mirror-MOT [15] uses four beams and a mirror as shown in Fig. 9b to reproduce the exact light-field configuration of the standard MOT in the half-space delimited by the mirror. It is similar (but not identical) to an earlier surface-MOT scheme using eight beams [82], and has also been related to the 'pyramid MOT' [83], which traps atoms inside a pyramid formed by four mirror surfaces. Note that, although other planar mirror orientations exist which reflect beams in the right directions, the configuration of Fig. 9 is the only one in which the reflected beams have the correct polarizations with respect to the magnetic quadrupole field.

To employ the mirror-MOT with a chip trap, the chip surface has to be reflective. This can be achieved either by adding a mirror layer on top of the conductor structure (cf. Sect. 3), or by using a chip that is completely metalized with the exception of narrow (~ 2–10-μm) gaps separating the conductors [69]. Remarkably, the deformation of the light field due to these gaps does not seem to result in a significant degradation of MOT performance.

The position of the MOT center can be displaced slightly by superposing an appropriate homogeneous magnetic field on the quadrupole field. When the center is located sufficiently far away from the surface (more than about 2 mm), the mirror-MOT achieves a performance comparable to a standard MOT. The chip currents are usually not sufficient to create a magnetic trap that far from the surface. For smaller distances, however, the mirror-MOT lifetime and steady-state atom number decrease, as shown in Fig. 10. To circumvent this problem, the MOT is loaded far from the surface where the atom number is high, then shifted and transferred into the chip trap within a few 10 ms, fast enough to avoid significant losses. To center the MOT at the exact location of the magnetic trap, without having to align the MOT coils with micrometric precision, an intermediate step can be used in which the MOT quadrupole field is generated on-chip. To provide higher wire currents for this on-chip MOT and for initial magnetic trapping, the setup can be improved by embedding a macroscopic wire below the chip surface [69]. (For the role of such a high-current wire in magnetic trap compression, see Sect. 5.1.3.)

Finally, to achieve good initial conditions for evaporative cooling, short phases of MOT compression, optical molasses, and optical pumping are inserted immediately before switching on the magnetic trap, just as in standard BEC experiments [84]. A detailed description with numerical values of all steps of this loading procedure is given in [15].

4.1.2 Loading by adiabatic transfer after precooling. As an alternative to direct transfer from a MOT, the chip trap can be loaded by magnetic transfer from a coil-based, intermediate magnetic trap. A particular and very effective implementation

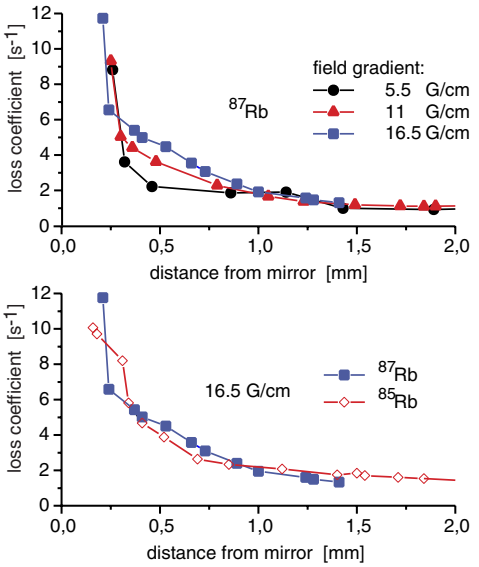

FIGURE 10 Loss coefficient of a mirror-MOT as a function of the distance from the mirror surface, measured under different conditions. Each point is extracted from a fit to a MOT charging–discharging curve. Discharging curves were obtained by first loading the MOT far away from the surface, then shifting the quadrupole center to the position specified in the graph. The cold-atom cloud quickly moves to the new position, followed by a slower decay of the atom number to a lower equilibrium value. In the *upper graph*, the loss coefficient in a ^{87}Rb MOT is traced for different values of the quadrupole field gradient. The *lower graph* shows data for ^{87}Rb and ^{85}Rb MOTs obtained with the same gradient. No significant difference is observed, which suggests that hyperfine state-changing collisions do not play a significant role in the loss process

of this method is demonstrated in [14], where it is used to achieve a Bose–Einstein condensate of 4×10^5 ^{87}Rb atoms in an extremely elongated chip trap. In this experiment, a multistep procedure – involving two pairs of coils, two auxiliary wires, and several stages of magnetic transfer – successively compresses and rf-cools the cloud before it is transferred into the chip trap. This rf precooling, which increases the phase-space density before transfer, helps to obtain a large atomic sample in the small volume of the chip trap.

In a very recent experiment [73], a far-detuned, focussed laser beam ('optical tweezers') has been used to transfer a sodium BEC from a 'production chamber' into a macroscopic wire trap located in a 'science chamber' 36-cm away. The same method can be used to load a chip trap. Although the complexity of such an experiment is considerably higher than with either magnetic transfer or direct loading, the advantages are better optical access to the chip trap and easy exchange of substrates without affecting the 'production' part of the setup.

In a comparison of all three methods, the mirror-MOT loading scheme is probably the simplest one, but it remains to be shown whether it can be used to obtain large samples. The need for a mirror layer on the chip may be a disadvantage in some applications, although the atoms can be transported away from the production region into a noncoated area by using a magnetic conveyor belt (Sect. 4.3.3). Magnetic transfer as described in [14] requires a better vacuum and a more sophisticated magnetic setup, but has been demonstrated to lead to larger samples, as does transfer by optical tweezers [73]. The latter method also provides easy sample exchange and good optical access, but is certainly the most

complicated of the three. Finally, other methods of magnetic transfer such as [85] may be adapted to load chip traps.

4.1.3 Continuous loading. To achieve a monochromatic atomic beam of high density and low transverse temperature, the experimentalist has at his disposal the same repertoire of methods that were discussed above (or their two-dimensional variants): magneto-optical cooling and confinement, optical pumping, magnetic compression, etc. New challenges arise because the temporal sequence of steps must be replaced by a spatial succession of regions along the beam axis. For methods such as rf-induced evaporative cooling, this means that the method has to be modified – in this case, the frequency sweep might be avoided by a variation of the magnetic potential along the beam axis. No standard has evolved yet for continuous loading. Although continuous-loading schemes have been used in a number of chip experiments [21, 23, 70], none of them aimed at a high coupling efficiency and a substantial collision rate. Thus, improvements are necessary (and possible) to achieve evaporative cooling in the waveguide [86], as may be required for external-state interferometers such as [74, 75]. Such experiments may benefit from current experiments that aim at evaporative cooling of atomic beams in macroscopic magnetic guides [87].

4.2 *Two-dimensional confinement: guiding experiments*

Because of the analogy with optical fibers, atom guides are a deceptively natural concept for matter-wave optics, and for atom interferometers in particular. A certain class of applications – which includes, in particular, gyroscopes – indeed seem to require the use of guides. But atomic matter waves can be stopped, and many fundamental operations, such as splitting and merging of wave packets, can be carried out with atoms of zero mean velocity. Using trapped atoms wherever possible leads to a smaller setup and avoids a number of problems that guiding experiments have to deal with. Indeed, the absence of control over the longitudinal motion is a complication for guiding experiments in the quantum regime. Moreover, techniques are still to be developed to achieve an atomic beam in a well-defined vibrational state of an atom guide, whereas established, reliable methods already exist for producing the equivalent state in a three-dimensional trap (i.e. a Bose–Einstein condensate). So far, all guiding experiments – with microstructures as well as with discrete wires – have been carried out with thermal atomic ensembles. However, as experimental techniques evolve, there is little doubt that the single-mode regime will ultimately be attained, enabling realization of devices such as integrated atomic gyroscopes. At this stage, the advantage of continuous loading will also come into play.

4.2.1 Demonstrations of guiding on a chip. The two first demonstrations of on-chip guiding were carried out in 1999 [21, 22], almost simultaneously with the first three-dimensional chip trap experiment [15]. Similar in their general ideas, but with a number of differences in the implementation, these experiments mainly demonstrated that laser-cooled atoms could indeed be coupled into the magnetic guides formed by current-carrying conductors on a chip, and that they could be transported over centimetric distances. The experiment in Boulder [21] used two parallel copper conductors ($100 \times 100\ \mu m^2$ cross section, 200-μm distance between centers) on a glass substrate. The field configuration was that of Fig. 5c, which allowed the researchers to guide the atoms around curves along a total distance of 10 cm in a horizontal direction. Atoms leaving the guide were detected by a hot-wire detector. The Harvard experiment [22] employed up to four parallel gold conductors with a spacing of 200 μm on a transparent sapphire substrate. Guiding was demonstrated with two different field configurations (Fig. 5b and d). The guiding direction was nearly vertical and could be adjusted by rotating the substrate about a horizontal axis normal to its surface. Atoms were detected by measuring absorption of a probe beam, which could be scanned below the exit of the guide. In both experiments, beam stops on the substrate were used to block the large background of unguided atoms. The effects of guiding were clearly observable in both experiments.

It is instructive to compare the loading techniques of the two experiments. The Boulder experiment used continuous loading of ^{87}Rb atoms from an LVIS ('low-velocity intense source') [88]. Essentially, this source is a MOT with a sub-mm hole in one of the retroflection mirrors, through which a cold-atom beam emerges. Its mean longitudinal velocity and transverse velocity spread were 10.1 m s^{-1} and 5 cm s^{-1}, respectively. The guiding substrate was mounted immediately behind this hole; optical pumping, or molasses cooling, or a tapered section at the guide entrance were not used. Consequently, of the initial LVIS flux of 5×10^8 s^{-1}, only 2×10^6 s^{-1} remained at the guide exit. By contrast, the Harvard experiment used a cesium MOT located above the guide as a pulsed atom source: a cloud of 10^8 atoms was released from the MOT to couple into the guide while in free fall. As pointed out in Sect. 4.1.3, a pulsed scheme facilitates efficient coupling into a trap or guide. Indeed, several provisions were made in the Harvard experiment to ameliorate this coupling: first, a short optical molasses phase further cools the atoms after release from the MOT. Next, they are optically pumped into the appropriate Zeeman state in a homogeneous magnetic field. Finally, this field is transformed into the guiding field in such a way as to allow adiabatic following of the atomic polarization. Unfortunately, the analysis does not appear to give the coupling efficiency of this scheme.

4.2.2 Beam switches and splitters. After the initial demonstrations of guiding, development in the beam experiments has focussed on beam splitters. As mentioned above, all experiments so far have used thermal atomic ensembles; the function of the splitters can be understood classically (like a Y-shaped piece connecting water pipes), and quantum effects do not contribute significantly to the results. Nevertheless, these experiments constitute first tests of some potentials that are being considered for integrated atom interferometers (cf. Sect. 6.3).

Both demonstrated beam splitters [23, 24] use the general approach of two initially separated guiding potentials which merge into one and then separate again. Another option, which has not yet been demonstrated experimentally,

would be to use a beam splitter based on tunneling as proposed in [89].

The experiment in Boulder [23] (similar in its setup to the guiding experiment [21] summarized above) uses two conductors approaching each other (Fig. 11) and the field configuration of Fig. 5a with an additional external field component along the guide axis to prevent spin-flip losses. Where the transverse spacing between the conductors is large, two separate minima exist, located above the individual conductors. For a smaller spacing, the two minima move closer to each other and merge into one. Thus, the layout of Fig. 11a forms a four-port device; in the experiment, atoms are initially coupled into only one of the input ports. The configuration of Fig. 11a, which was used in the beam-splitting experiment described in [24], also has four ports despite the appearance of the conductor layout. Here the fourth port, located on the input side, leads diagonally towards the surface. In the experiment, the guide was loaded from the three-dimensional chip trap described above [69]; when the longitudinal confinement is removed, the atom cloud expands into the Y-shaped wire due to its longitudinal velocity spread. In both experiments, a variable splitting ratio was demonstrated; in the Boulder experiment, interesting additional measurements characterize the transverse nonadiabatic heating. Finally, in another experiment in Boulder [70], a more elaborate guide configuration was used to switch the flux of an input guide between two outputs.

Quantum-mechanically, the splitting ratio in waveguide splitters is determined by the dynamic evolution of the wave functions in the single-guide region as they propagate into the two-guide region. This ratio will generally depend on both longitudinal and transverse states, and on the geometry (in particular, the symmetry) of the splitting potential; moreover, reflections may also occur. None of the above configurations is ideal in this respect. The Y-shaped splitter, in particular, fundamentally suffers from the asymmetry due to the different angles between the two output conductors and the external field, leading to nonsymmetric output ports. The existence of the fourth port which can cause losses is another complication in this scheme. These problems are discussed in [24] and in more detail in [68], where some improved versions are also proposed. There is little doubt that coherent beam splitting on a chip will be demonstrated in the near future. The interferometers that can then be built possess the advantages of miniaturization that have already been pointed out. Whether they can become high-precision instruments is an open question; the main challenge will certainly be to master magnetic field fluctuations.

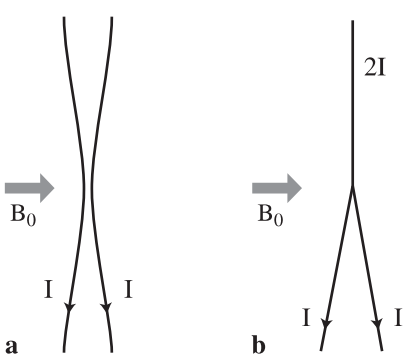

FIGURE 11 Guide configurations that have been used to split guided thermal beams. **a** Two separate wires with a closely spaced region to induce the coupling [23]. **b** A Y-shaped wire [24]

4.3 *Experiments with trapped thermal clouds*

4.3.1 Three-dimensional trapping on a chip. Three-dimensional trapping is the first step for all experiments with full control over the spatial degrees of freedom, and for Bose–Einstein condensation in particular. The first experiments [15, 69] have used the U-shaped and Z-shaped wire configurations introduced above (Sect. 2.2.2) and the mirror-MOT loading technique (Sect. 4.1.1). The planar IP trap designs contained in the 1995 study [16] have been built [65], but have not been used in any experiment published so far. In these designs, the trap center is located above a conductor-free region of the chip, which makes them interesting for some future applications.

4.3.2 Splitting and merging of trapped clouds. An experiment has been performed in Munich which demonstrates splitting and merging of thermal clouds, analogous to the experiments described in Sect. 4.2.2, but with trapped atoms [71, 90]. Here the mean velocity of the atoms is zero, and instead of a variation along some spatial guide axis, the potential varies along the time axis. This allows, for example, long-time splitting to pick up phase shifts without a growing size of the apparatus and the associated shielding and stability problems. Arbitrary numbers of splitting and merging cycles can be performed with the same simple conductor configuration.

A conductor layout for splitting and merging two Ioffe–Pritchard traps is shown in Fig. 12. By appropriately choosing

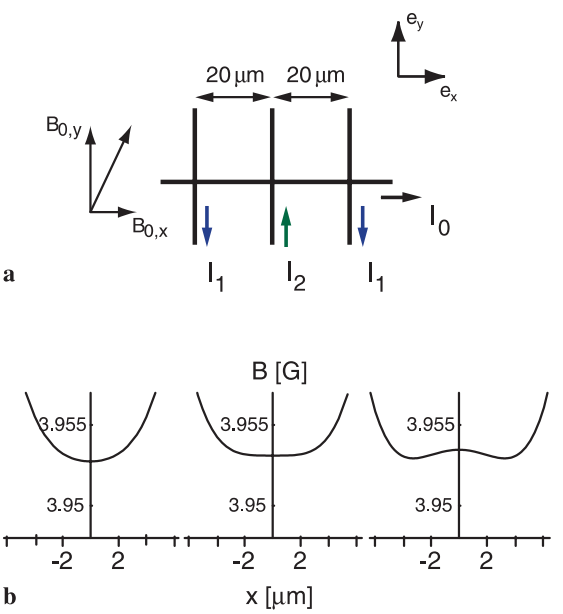

FIGURE 12 **a** Conductor layout to create the potential for a trapped-atom interferometer. **b** Potential created by this structure for $B_{0,x} = 1.6$ mT, $B_{0,y} = 2$ mT, $I_0 = 525$ mA, and the following values of I_1 and I_2: *left*: (140 mA, 0.25 mA); *center*: (142.04 mA, 3.33 mA); *right*: (142.91 mA, 4.65 mA)

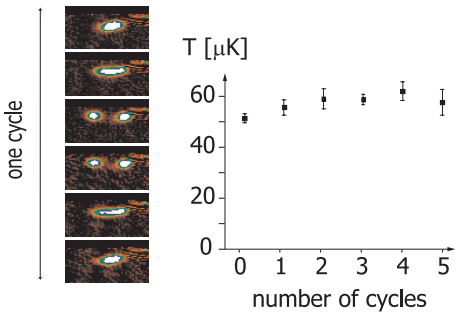

FIGURE 13 *Left*: absorption images of a thermal cloud of Rb atoms being split, then merged again by a potential similar to the one shown in Fig. 12. *Right*: resulting temperature of the atom cloud when the cycle (shown *left*) is executed up to five times

the currents, either a single- or a double-potential well is obtained. The potential used in the experiment was obtained with the conductors of the magnetic conveyor belt [71], and was used to split and merge two clouds each containing $\sim 10^5$ atoms at a temperature of $\sim 50\,\mu$K (Fig. 13). As in the case of the guiding experiment, this is a 'multimode' experiment due to the thermal distribution of the atoms. However, this experiment gave easy access to the temperature of the atom cloud by performing time-of-flight measurements. Thus, it was possible to verify the adiabaticity of the process by measuring the temperature before and after the splitting. Figure 13 shows the result for up to five complete splitting and merging cycles. The number of atoms did not decrease and the temperature remained constant to within the measurement accuracy of $\sim 1\,\mu$K, confirming the adiabaticity within these limits. This encouraging result raises hopes that a trapped-atom interferometer (cf. Sect. 6.3 below) can be realized with this splitting method.

4.3.3 Adiabatic transport with the 'atomic conveyor belt'. Trapped atoms can be transported parallel to the substrate surface with the 'atomic conveyer belt'. The magnetic potential for this device and the wire layout used to create it are shown in Fig. 14a and b. When time-dependent currents are applied as specified in the figure caption, the minima move to the right with the average speed l/T.

Figure 14c shows a sequence of absorption images which experimentally demonstrates the atomic transport in the potential of Fig. 14b. (As the imaging is destructive, the whole sequence of magneto-optic trapping, transfer to the magnetic trap, and magnetic transport is repeated for each picture.) Initially, the two leftmost minima have been populated with atoms from the MOT. During the transport, the two trapped clouds move to the right in accordance with the calculated potential.

This device may prove its usefulness in applications such as controlled coupling of trapped atoms to the quantized light field of a high-finesse resonator (e.g. a Fabry–Perot cavity [32] or a silica microsphere [91]). As discussed below in Sect. 5.3, the device can even transport a Bose–Einstein condensed cloud.

4.3.4 Other experiments with trapped thermal clouds. The wire layout of the atomic conveyor belt has turned out to be versatile enough for many other atom-manipulation devices that had not even been thought of when the conveyor substrate was fabricated. One example is an Ioffe–Pritchard trap with a rotatable axis, shown above in Fig. 7. Other examples include a 'linear collider' for cold neutral atoms [25] and a mechanism to refill an IP trap without loss of phase-space density [90].

5 Chip trap experiments II: Bose–Einstein condensation on a chip

Chip traps have been around since late 1998 [15] and have shown their versatility in a number of demonstration experiments (Sect. 4). It was the demonstration of an on-chip BEC [13, 14], however, which led to an explosion of interest in this method. Indeed, the chip technique dramatically simplifies the experimental effort that is necessary to obtain a Bose–Einstein condensate. It eliminates high-power,

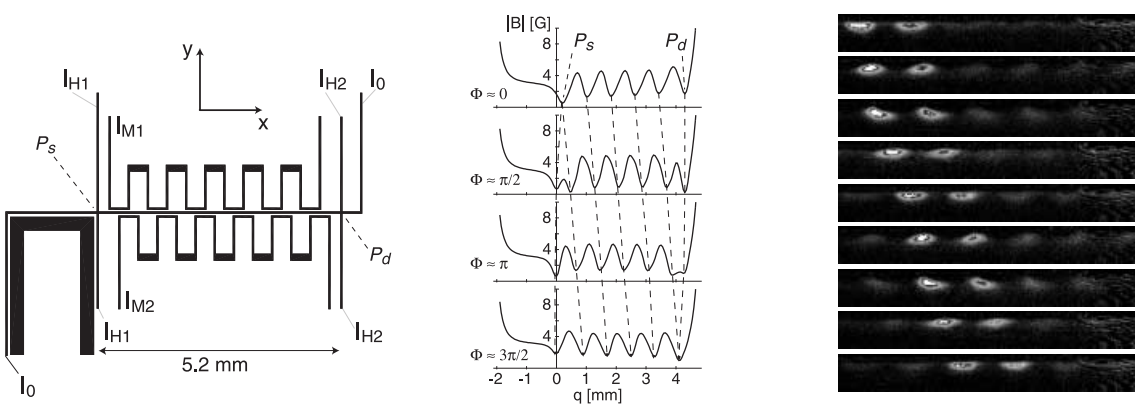

FIGURE 14 **a** Wire layout for the 'atomic conveyer belt'. The spatial period of the undulating wires is $l = 800\,\mu$m. **b** Magnetic potential produced by this layout with a constant field $\boldsymbol{B}_0 = 3\,\mathrm{G}\,\boldsymbol{e}_x + 16\,\mathrm{G}\,\boldsymbol{e}_y$ and the following currents: $I_0 = 1.5\,\mathrm{A}$, $I_{\mathrm{M1}} = 0.8\,\mathrm{A}\cos\phi$, $I_{\mathrm{M2}} = 0.8\,\mathrm{A}\sin\phi$, $I_{\mathrm{H1}} = -0.17\,\mathrm{A} + 0.15\,\mathrm{A}\cos\phi$, $I_{\mathrm{H2}} = -0.25\,\mathrm{A} + 0.18\,\mathrm{A}\sin\phi$. (In the experiment the phase is time-dependent, $\phi = 2\pi t/T$, with period T). The coordinate q follows the path of the transverse (yz plane) minimum for each value of the longitudinal x coordinate. **c** Sequence of absorption images showing the transport of cold trapped atoms in this potential. The probe beam is directed along the y axis (hence, parallel to the substrate surface). The period is $T = 100$ ms; for each image, the transport phase is 25 ms longer than for the preceding one

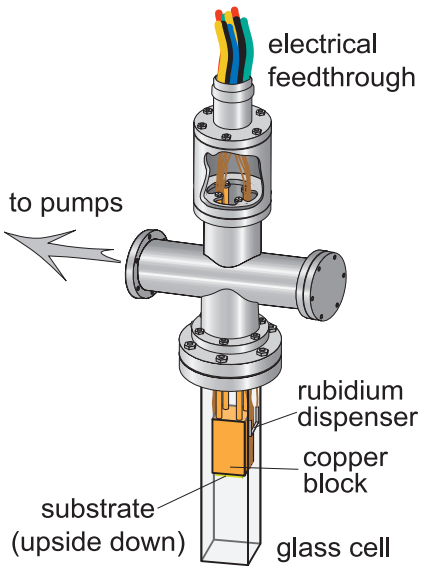

FIGURE 15 Vacuum system used in the Munich chip trap experiment [13]. Because of the efficient evaporation in the chip trap, this very simple setup is sufficient to achieve a BEC. The substrate is mounted facing downwards, so that the atom cloud may be released to expand in free fall (time-of-flight analysis)

water-cooled magnetic coils and large power supplies, and requires neither differential pumping nor (at least in the case of ^{87}Rb) atomic beams [13, 14] (Fig. 15). In combination with direct loading from a mirror-MOT, it also greatly accelerates the condensate-production rate – from typically more than a minute to less than ten seconds – and relaxes the vacuum requirements by about two orders of magnitude [13]. No more than three diode lasers are required to obtain a coherent matter wave by this method. Along with these advantages, the wide array of integrated manipulation capabilities comes for free.

This section presents some specific methods and issues pertaining to on-chip condensates that were only touched upon in the two first chip BEC reports [13, 14]. For a more general introduction to properties of atomic BECs and the associated techniques, the reader is referred to excellent reviews, such as [92, 93] and [94, 95], on evaporative cooling. Likewise, the results of the two chip BEC experiments are only briefly summarized here; a more exhaustive description can be found in [13, 14].

5.1 *Special techniques*

5.1.1 Modulating the background pressure. As an alternative to a reservoir containing a quantity of an elementary alkali metal, there exist so-called alkali metal 'dispensers', about the size of a match, which contain some milligrams of the alkali in a chemical compound, and can be used for MOT loading [36]. When the dispenser is heated by running a current of a few amperes through its metal housing, the elementary alkali is evaporated (along with some other contaminating elements). This method has several advantages. The dispenser can be stored and installed in air, without most of the safety measures that are necessary when dealing with elementary alkalis. More importantly, the vapor pressure can be adjusted on a time scale of the order of 10 s, much faster than with an oven. When the base pressure in the cell is low enough to achieve a trap lifetime significantly longer than this, it becomes possible to modulate the alkali partial pressure during the experimental cycle, using a high partial pressure for loading, then switching off the dispenser to achieve a good trap lifetime [96]. This was done in the Tübingen experiment [14], where the background pressure is below 2×10^{-11} mbar. The Munich experiment has much smaller pumps, and the higher background pressure leads to a magnetic trap lifetime below 10 s, so that dispenser switching is not useful. However, it was found that another technique allowed a still faster modulation of the rubidium pressure: light-induced desorption [97] using a standard halogen bulb placed close to the glass cell.

5.1.2 Loading large samples into chip traps. In traditional BEC experiments, care is taken to load as many atoms as possible into the magnetic trap (often 10^9 atoms or more), because this facilitates evaporative cooling, which is a difficult process even at the typical ultra-low pressures below 10^{-11} mbar. In chip traps, with their much stronger compression and correspondingly higher collision rate, evaporative cooling is a much more robust process. In the Munich experiment, evaporative cooling to condensation succeeds in spite of an initial atom number of only a few 10^6 atoms and a base pressure in the upper 10^{-10}-mbar range. Nevertheless, a higher initial atom number is obviously useful if a large condensate is desired. Some methods for increasing this number were already discussed in Sect. 4.1. In spite of the obvious limitation of the chip trap volume (cf. Fig. 2), current experiments remain far below the limits that could achieved with some straightforward improvements. First of all, the trap volume strongly depends on the wire current, which can be increased by a large factor by using an embedded, thick wire as described in [69] (cf. Sect. 4.1.1), or by adding a larger conductor on the chip. Another approach, which does not need higher currents, would be to start with an elongated MOT and magnetic trap, followed by longitudinal compression with a scheme as shown in Fig. 16.

5.1.3 Trap compression. The extreme 'compressibility' of chip traps has already been pointed out. Compression plays a crucial role in BEC experiments because it increases the collision rate γ, which sets the time scale for evaporative cooling:

$$\gamma = n\sigma\bar{v}\,, \tag{23}$$

where n is the density, σ the elastic scattering cross section, and $\bar{v}$ the mean velocity. Adiabatic compression increases both n and $\bar{v}$. (In fact, even a sudden compression can still increase γ.) This method of increasing the collision rate only comes to a halt when the density is so high that three-body collisions become an important loss term. In macroscopic traps, densities that high usually occur only after substantial evaporative cooling, whereas chip traps may achieve this by mere compression immediately after loading. Thus, chip traps can achieve the fastest evaporation that is fundamentally allowed by this constraint on density.

Another potential loss factor that has to be considered is 'spilling over' of the compressed trap. Obviously, the higher temperature after compression requires a deeper trap (3).

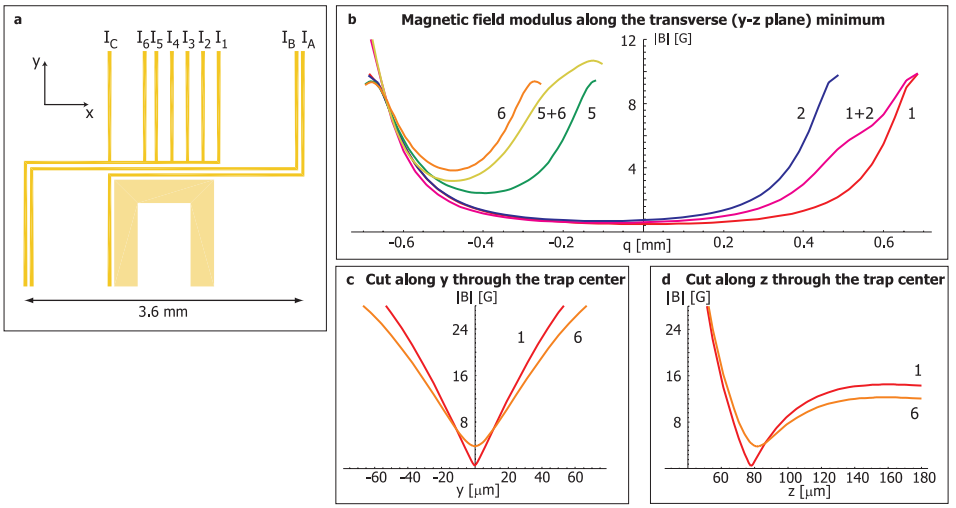

FIGURE 16 **a** Conductor layout for an Ioffe–Pritchard trap with adjustable aspect ratio, requiring no external fields. **b**, **c**, and **d** Potentials generated by these conductors. For all curves, $I_A = I_B = 2$ A. Another current of 2 A flows through the conductors corresponding to the *labels* of the individual curves. As this third current is blended from I_1 to I_6, the longitudinal trap frequency increases from 140 Hz to 320 Hz. At the same time, the transverse frequency changes from 11 kHz to 3.2 kHz. Note that a similar but stronger trap can be realized with an external field as in Fig. 2 and $I_A = I_B = 0$

While the exact temperature increase in a realistic potential (such as the one of Fig. 2) is difficult to compute, there exist analytical results [94] for all relevant quantities in power-law potentials in d dimensions,

$$U(r) \propto r^{\frac{d}{\delta}}. \tag{24}$$

If the potential is multiplied ('compressed') by a factor α, the temperature scales as

$$T \propto \alpha^{\frac{2\delta}{2\delta+3}}. \tag{25}$$

When a 'Z-trap' is compressed adiabatically by slowly increasing the bias field from B_{0i} to $B_{0f} = \beta B_{0i}$ as in Fig. 2, the trap depth (being proportional to B_0 if we neglect the small bias field in the trap center) also increases by a factor β. To obtain a crude estimate of the concomitant temperature increase, let us approximate the process as the compression of a two-dimensional, linear potential ($d = \delta = 2$, $T \propto \alpha^{4/7}$). If we further estimate the compression factor by the ratio of the initial and final transverse gradients near the trap center (9),

$$\alpha \sim \frac{B_f'(r_0)}{B_i'(r_0)} = \beta^2,$$

we find a temperature increase $T \propto \beta^{8/7}$, only slightly faster than the trap depth. Within this crude model, the trap will remain about 'as full' as it was before compression, and boiling out of the trap will not become a major loss factor due to the compression, which is a reassuring result.

Note that, in view of the spill-over problem, compressing the trap by increasing B_0 is certainly a better choice than reducing I. The latter method also leads to trap compression, but leaves the trap depth unchanged. Thus, unless the initial η was very large, such a compression will present significant losses.

Limit in trap depth. The simplification made above, to identify the external field B_0 with the trap depth, has some limits that should not be forgotten. First, the contribution of gravity to the total potential has been neglected: the restoring force in the vertical direction vanishes when the magnetic gradient becomes as low as $B' = mg/\mu_m$ (0.15 T/m for our Rb example state). In steep traps, the effect of this correction is small. When the trap is very strongly compressed by increasing B_0, on the other hand, the finite field at the wire surface must be taken into account; for a wire of finite width, this is

$$B_s = \frac{\mu_0}{2}\frac{I}{w} - B_0\,. \tag{26}$$

Thus, B_s limits the trap depth only when $z \lesssim w$.

5.1.4 Surface-induced evaporation. The presence of the chip surface enables a new evaporation method to be used, first demonstrated in [15] and called surface-induced evaporation. In this method, atoms with an energy in the z direction in excess of the potential at the surface are removed from the trap by collisions with the surface. In its first demonstration, a quadrupole trap with a short lifetime was used

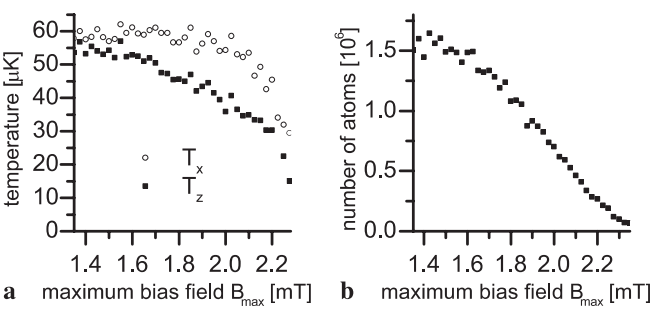

FIGURE 17 Surface-induced evaporation. While the wire current is kept constant at 1.6 A, the bias field is ramped up to a final value B_{max} within 100 ms. 2-ms later, the trap is shifted back, within another 100 ms, to a distance of $z = 300\,\mu$m from the surface ($I = 2$ A, $B_0 = 0.9$ mT), where the trap parameters can be measured as a function of B_{max} under identical conditions. **a** Temperature of remaining atoms after shifting the cloud towards the surface by increasing B_0 up to B_{max}, then shifting it back to a constant measurement position. (Due to decreasing density, thermalization during the back-shifting process is not complete. The change in trap aspect ratio during shifting therefore leads to a difference between transverse and longitudinal temperatures.) **b** Number of atoms remaining in the trap after the shifting sequence. The decrease is only partly due to the surface-induced evaporation; in the quadrupole trap, the compression of the trap also results in an increased loss rate due to Majorana spin flips. Nevertheless, the phase-space density grows by more than a factor of two. A more detailed description of this experiment is given in [15]

(Fig. 17). Current chip BEC experiments have not yet explored the use of surface-induced evaporation. Although the dimensionality of the evaporation is reduced, it will be interesting to explore this method further, because of its properties which distinguish it from the standard rf-induced evaporation. Apart from the simplification (no need for rf source and control), another feature is that it can be applied locally.

5.2 *Experimental results*

The two first chip BEC experiments used standard rf-induced evaporation to achieve condensation. The detailed experimental sequence for each experiment can be found in [13, 14]. The final result in the Tübingen experiment, achieved with a total evaporative cooling time of 27 s, is a condensate containing 4×10^5 atoms in a potential with radial and axial frequencies of 840 Hz and 14 Hz, respectively. No heating of the condensate was observed; the condensate lifetime in a relaxed potential was 1 s, and an rf shield had no effect. In the Munich experiment, a very short evaporation could be used due to the direct loading, which enabled strong initial compression (Fig. 18). The condensate forms despite an observed heating rate of more than 1 μK s^{-1}. This heating is believed to be mainly due to current noise; indeed, the current sources used in Munich have been measured to produce significantly more noise than the ultra-low-noise sources used in Tübingen. Nevertheless, condensation is achieved, and the condensate lifetime is 500 ms without an rf shield. Two trapping field configurations with different aspect ratios were used: one with frequencies $\nu_{x,y,z} = (20, 3900, 3900)$ Hz (frequency ratio 200 : 1), the other with frequencies $\nu_{x,y,z} = (300, 3400, 3500)$ Hz (ratio 12 : 1). In both cases, the rf cooling time was typically 2 s and could be made as short as 700 ms. This is more than an order of magnitude faster than in the usual BEC experiments; the total cycle time (including MOT loading, etc.) was 10 s or shorter. The number of condensed atoms well below the transition temperature was about 3000 in both configurations. Higher numbers can be expected if the source of the heating can be eliminated.

5.3 *Condensate transport with the conveyor belt*

As a first demonstration of the power of the new method, an on-chip condensate has been transported over a distance of 1.6 mm with the atomic conveyor belt described above in Sect. 4.3.3. This is accomplished simply by producing a condensate in the starting position of the conveyor, then applying periodic modulation currents to move the potential (cf. Sect. 4.3.3). The result is shown in Fig. 19. The fact that the delicate condensate 'survives' this procedure is a very encouraging result in view of applications such as the trapped-atom interferometer described below.

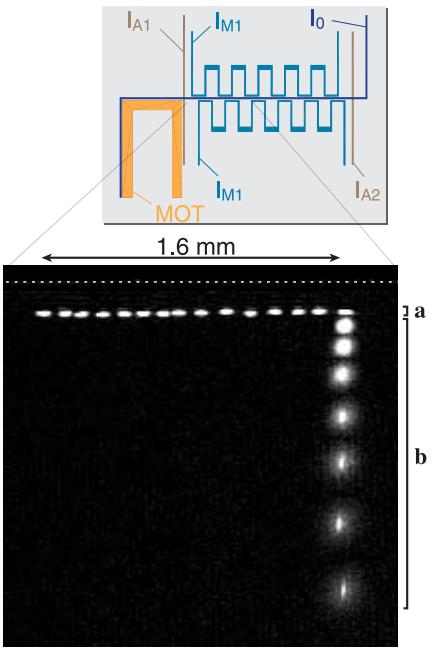

FIGURE 19 Transport of a BEC on the magnetic conveyor belt. *a* Superposed absorption images taken at fixed time intervals during transport. The distance between the first and last images is 1.6 mm; the transport time is 100 ms. The line of sight is parallel to the *y* axis (cf. Fig. 14); the *dashed line* marks the edge of the substrate. *b* Time-of-flight images of the atom cloud after release at the final position, exhibiting the bimodal structure characteristic of a BEC. The maximum expansion time (*bottom image*) is 19.3 ms

6 Future prospects

Experiments are now under way in many laboratories that will explore the new possibilities and applications of chip potentials. From interferometers to magnetic lattices, it is easy to imagine wire layouts that create complex and

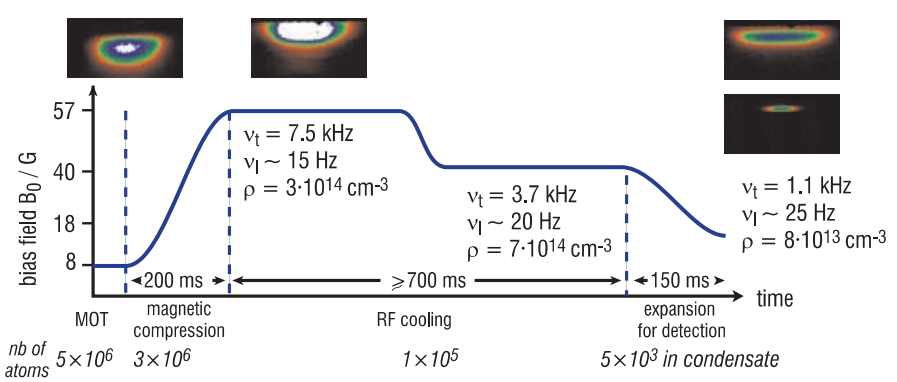

FIGURE 18 Temporal variation of the external bias field used for evaporative cooling to a BEC in the Munich chip trap

FIGURE 20 Photographs of various chip trap substrates (gold on AlN, original size 10.7 mm × 7.1 mm each). From *left* to *right*: quadrupole traps and Ioffe–Pritchard traps of various aspect ratios; the atomic conveyor belt; guides with electrical field electrodes between Y-shaped splitting and recombining regions; magnetic lattice structure. All four substrates were produced in Munich in 1999; to date, only the first two have been used in experiments

possibly useful potentials (Fig. 20). The following paragraphs briefly discuss some of the applications on which experimental progress can be expected in the near future.

6.1 *Surface interactions*

In chip traps, the distance of a coherent matter wave from a solid-state surface can be controlled with submicrometric precision. This high degree of control enables a new kind of surface studies. At the same time, surface effects will also impose the ultimate limits to the trap–surface distance in matter-wave manipulation experiments. Experimentally, it is still unknown at which distance and by which mechanisms the surface becomes a dominant source of losses, heating, and decoherence. In the BEC experiment in Tübingen, no heating was observed at a trap–surface distance of 100 μm, putting an upper limit of 100 nK/s on the heating rate in this trap. The trap lifetime was 1 s at a trap–surface distance of 20 μm [98]. A thorough theoretical analysis of trap loss, heating, and decoherence induced by the surface has been published in a recent series of articles [18–20]. According to these results, surface effects become important at distances between 10 and 1 μm. Experiments will soon be able to verify these predictions.

6.2 *Condensates in unusual potentials*

Due to the ease with which elongated traps can be prepared and adjusted, the chip trap condensates lend themselves to studies of the interesting regime of fluctuating phase [27, 28]. Furthermore, effects of reduced dimensionality [26, 29] may become observable in chip traps with correspondingly optimized parameters. Another fundamental system to which chip traps are well adapted is a generic double-well potential with adjustable coupling. In combination with single-atom detectors, the number of atoms in each well would be accessible to direct counting. Here, a small spacing (in the 1-μm range) between the individual wells is required to achieve substantial coupling. In this and other applications where a small characteristic size of the potential is essential, a smaller atom–surface distance than in today's experiments will probably be required.

6.3 *Integrated atom interferometers*

Besides its use in fundamental measurements, atom interferometry is expected to increase the sensitivity of gravity gradiometers and gyroscopes by several orders of magnitude over established technologies [99]. For these applications, robust and portable devices must now be developed. Chip guides and traps have been considered from the beginning as possible implementations of such interferometers. Indeed, miniaturization and robustness are obvious advantages of this technology. Experiments must show whether the difficulty of working in a state with nonvanishing magnetic moment can be mastered to a sufficient degree for such high-precision applications. On-chip interferometers have also been proposed for other tasks. In an interferometer potential with strong transverse confinement, the phase shift due to a controlled collision between two atoms could be measured [34, 35, 100]. Such an interferometer forms the central part of a two-qubit 'phase gate' for quantum information processing with neutral atoms in microtraps [34, 35].

Various configurations have been studied theoretically for observing interferences of vibrational states in miniature magnetic guides and traps [74, 75, 101, 102]. Now that on-chip condensates are available, such external-state atom interferometers become a realistic goal for experiments. In these schemes, the splitter device of Fig. 12 [102] or a similar device for guided atoms [74] is used to divide an atomic wave packet, initially in the vibrational ground state, into two coherent, but spatially separated lobes, which form the 'arms' of the interferometer. In the most recent proposal [75], an interference pattern is calculated to persist even when multiple transverse vibrational modes are populated. The interferometer is sensitive to additional potentials that induce a phase shift between the two arms, such as electric and magnetic field gradients, or a local interaction with another atom placed close to one of the arms. For symmetry reasons, the effect of such a phase shift is to transfer part of the atomic probability distribution into an excited vibrational state when the split potential is transformed back into a single well. This mechanism is depicted in Fig. 21. A crucial issue in such interferometer schemes is the

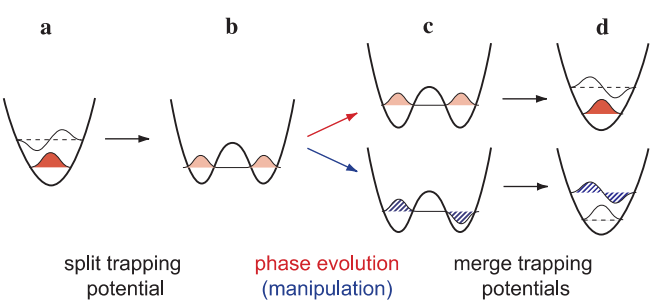

FIGURE 21 Scheme of the trapped-atom interferometer: one or several atoms are prepared in the vibrational ground state of the single-well potential (**a**). When the well separates, the wave function evolves adiabatically into a symmetric delocalized state (**b**). The phase of the wave function in each potential well evolves independently and monitors sensitively external electric and magnetic field gradients (**c**). As the potential wells reunite, the antisymmetric state evolves into the first exited vibrational state, whereas the symmetric one transforms back into the ground state

suppression of unwanted excitations, which could be induced either by stray-field gradients or by the splitting process itself if it is not completely adiabatic. The latter contribution can be reduced by performing the potential transformation sufficiently slowly. One-dimensional simulations [102] indicate that this can be done without going to unrealistically slow time scales: the whole process can be performed in less than 100 ms with a probability for unwanted excitations below 10^{-3}. Thus, phase noise and decoherence due to stray fields and current fluctuations remain as the crucial issue. Experiments are required to show whether sufficient control over these effects can be achieved.

6.4 *Integration of optical resonators*

With the magnetic conveyor belt, single atoms and small condensates can be positioned with a precision much better than an optical wavelength. By developing optical resonators that are compatible with the chip technique, it will be possible to shift a trapped atom or small condensate into the resonator and to position it precisely in the standing wave inside the resonator [103], achieving well-defined coupling and long interaction times.

Not only will such techniques lead to robust and simple detectors with single-atom detection efficiency [104–106] – it is not unreasonable to envisage, moreover, cavity quantum electrodynamics experiments using chip technologies [107].

6.5 *Outlook*

Besides the applications discussed above, a straightforward use of the chip technique is as a simple and robust source of cold atoms and condensates. Such a source can be of interest in atomic fountain clocks [108], for example. The field further expands when other techniques are integrated on the chip – such as optical detectors, or even optical waveguides [67]. State-dependent potentials can be constructed by adding charged wires creating strong electric fields, and well-developed theoretical studies exist which describe quantum information processing with neutral atoms in such integrated traps [34, 35]. Experiments are now starting to explore this fascinating realm.

ACKNOWLEDGEMENTS I am indebted to T.W. Hänsch for inspiring discussions, to J. Thywissen, P. Hommelhoff, and W. Hänsel for careful proofreading and lucid remarks on the manuscript, and to all members of the Munich chip trap team for their support.

REFERENCES

1 M.H. Anderson, J.R. Ensher, M.R. Matthews, C.E. Wieman, E.A. Cornell: Science **269**, 198 (1995)
2 K.B. Davis, M.-O. Mewes, M.R. Andrews, N.J. van Druten, D.S. Durfee, D.M. Kurn, W. Ketterle: Phys. Rev. Lett. **75**, 3969 (1995)
3 C.C. Bradley, C.A. Sackett, R.G. Hulet: Phys. Rev. Lett. **78**, 985 (1997)
4 M.R. Matthews, B.P. Anderson, P.C. Haljan, D.S. Hall, C.E. Wieman, E.A. Cornell: Phys. Rev. Lett. **83**, 2498 (1999)
5 K.W. Madison, F. Chevy, W. Wohlleben, J. Dalibard: Phys. Rev. Lett. **84**, 906 (2000)
6 J.R. Abo-Shaeer, C. Raman, J.M. Vogels, W. Ketterle: Science **292**, 476 (2001)
7 M.R. Andrews, C.G. Townsend, H.J. Miesner, D.S. Durfee, D.M. Kurn, W. Ketterle: Science **275**, 637 (1997)
8 I. Bloch, T.W. Hänsch, T. Esslinger: Nature **403**, 166 (2000)
9 M.-O. Mewes, M. Andrews, D. Kurn, D. Durfee, C. Townsend, W. Ketterle: Phys. Rev. Lett. **78**, 582 (1997)
10 B.P. Anderson, M. Kasevich: Science **282**, 1686 (1998)
11 I. Bloch, T.W. Hänsch, T. Esslinger: Phys. Rev. Lett. **82**, 3008 (1999)
12 E.W. Hagley, L. Deng, M. Kozuma, J. Wen, K. Helmerson, S.L. Rolston, W.D. Phillips: Science **283**, 1706 (1999)
13 W. Hänsel, P. Hommelhoff, T.W. Hänsch, J. Reichel: Nature **413**, 498 (2001)
14 H. Ott, J. Fortagh, G. Schlotterbeck, A. Grossmann, C. Zimmermann: Phys. Rev. Lett. **87**, 230401 (2001)
15 J. Reichel, W. Hänsel, T.W. Hänsch: Phys. Rev. Lett. **83**, 3398 (1999)
16 J.D. Weinstein, K.G. Libbrecht: Phys. Rev. A **52**, 4004 (1995)
17 M.D. Barrett, J.A. Sauer, M.S. Chapman: Phys. Rev. Lett. **87**, 010404 (2001)
18 C. Henkel, M. Wilkens: Europhys. Lett. **47**, 414 (1999)
19 C. Henkel, S. Pötting, M. Wilkens: Appl. Phys. B **69**, 379 (1999)
20 C. Henkel, S. Pötting: Appl. Phys. B **72**, 73 (2001)
21 D. Müller, D.Z. Anderson, R.J. Grow, P.D.D. Schwindt, E.A. Cornell: Phys. Rev. Lett. **83**, 5194 (1999)
22 N.H. Dekker, C.S. Lee, V. Lorent, J.H. Thywissen, S.P. Smith, M. Drndić, R.M. Westervelt, M. Prentiss: Phys. Rev. Lett. **84**, 1124 (2000)
23 D. Müller, E.A. Cornell, M. Prevedelli, P.D.D. Schwindt, A. Zozulya, D.Z. Anderson: Opt. Lett. **25**, 1382 (2000)
24 D. Cassettari, B. Hessmo, R. Folman, T. Maier, J. Schmiedmayer: Phys. Rev. Lett. **85**, 5483 (2000)
25 J. Reichel, W. Hänsel, P. Hommelhoff, T.W. Hänsch: Appl. Phys. B **72**, 81 (2001)
26 M. Olshanii: Phys. Rev. Lett. **81**, 938 (1998)
27 D.S. Petrov, G.V. Shlyapnikov, J.T.M. Walraven: Phys. Rev. Lett. **87**, 050404 (2001)
28 S. Dettmer, D. Hellweg, P. Ryytty, J.J. Arlt, W. Ertmer, K. Sengstock, D.S. Petrov, G.V. Shlyapnikov, H. Kreutzmann, L. Santos, M. Lewenstein: Phys. Rev. Lett. **87**, 160406 (2001)
29 A. Görlitz, J.M. Vogels, A.E. Leanhardt, C. Raman, T.L. Gustavson, J.R. Abo-Shaeer, A.P. Chikkatur, S. Gupta, S. Inouye, T. Rosenband, W. Ketterle: Phys. Rev. Lett. **87**, 130402 (2001)
30 J.M. Raimond, M. Brune, S. Haroche: Rev. Mod. Phys. **73**, 565 (2001)
31 D.W. Vernooy, A. Furusawa, N.P. Georgiades, V.S. Ilchenko, H.J. Kimble: Phys. Rev. A **57**, R2293 (1998)
32 P.W.H. Pinkse, T. Fischer, P. Maunz, G. Rempe: Nature **404**, 365 (2000)
33 P.R. Berman (Ed.): *Atom Interferometry* (Academic, Boston, MA 1997)
34 T. Calarco, E.A. Hinds, D. Jaksch, J. Schmiedmayer, J.I. Cirac, P. Zoller: Phys. Rev. A **61**, 022304 (2000)
35 H.-J. Briegel, T. Calarco, D. Jaksch, J.I. Cirac, P. Zoller: J. Mod. Opt. **47**, 415 (2000)
36 J. Fortagh, A. Grossmann, C. Zimmermann, T.W. Hänsch: Phys. Rev. Lett. **81**, 5310 (1998)
37 J. Denschlag, D. Cassettari, J. Schmiedmayer: Phys. Rev. Lett. **82**, 2014 (1999)
38 M. Key, W. Rooijakkers, E.A. Hinds: New J. Phys. **2**, 25.1 (2000)
39 J.A. Sauer, M.D. Barrett, M.S. Chapman: Phys. Rev. Lett. **87**, 270401 (2001)
40 G.I. Opat, S.J. Wark, A. Cimmino: Appl. Phys. B **54**, 396 (1992)
41 D.C. Lau, A.I. Sidorov, G.I. Opat, R.J. McLean, W.J. Rowlands, P. Hannaford: Eur. Phys. J. D **5**, 193 (1999)
42 L. Cognet et al.: Europhys. Lett. **47**, 538 (1999)
43 P. Rosenbusch, B.V. Hall, I.G. Hughes, C.V. Saba, E.A. Hinds: Phys. Rev. A **61**, 031404(R) (2000)
44 This discussion mainly follows [84]
45 K.-J. Kügler, W. Paul, U. Trinks: Phys. Lett. **72B**, 422 (1978)
46 A.L. Migdall, J.V. Prodan, W.D. Phillips, T.H. Bergeman, H.J. Metcalf: Phys. Rev. Lett. **54**, 2596 (1985)
47 V.S. Bagnato, G.P. Lafyatis, A.G. Martin, E.L. Raab, R.N. Ahmad-Bitar, D.E. Pritchard: Phys. Rev. Lett. **58**, 2194 (1987)
48 H.F. Hess, G.P. Kochanski, J.M. Doyle, N. Masuhara, D. Kleppner, T.J. Greytak: Phys. Rev. Lett. **59**, 672 (1987)
49 R. van Roijen, J.J. Berkhout, S. Jaakkola, J.T.M. Walraven: Phys. Rev. Lett. **61**, 931 (1988)
50 W.H. Wing: Prog. Quantum Electron. **8**, 181 (1984)
51 W. Ketterle, D.E. Pritchard: Appl. Phys. B **54**, 403 (1992)
52 E. Majorana: Nuovo Cimento **9**, 43 (1932)
53 T. Bergeman, G. Erez, H.J. Metcalf: Phys. Rev. A **35**, 1535 (1987)
54 K.B. Davis, M.O. Mewes, M.A. Joffe, W. Ketterle: In: 14th Int. Conf.

At. Phys., Book Abstr. (University of Colorado, Boulder, CO 1994) p. 1–M3
55 W. Petrich, M.A. Anderson, J.R. Ensher, E.A. Cornell: In *14th Int. Conf. At. Phys., Book Abstr.* (University of Colorado, Boulder, CO 1994) p. 1–M7
56 W.D. Phillips, J.V. Prodan, H.J. Metcalf: J. Opt. Soc. Am. B **2**, 1751 (1985)
57 K.B. Davis, M.-O. Mewes, M.A. Joffe, M.R. Andrews, W. Ketterle: Phys. Rev. Lett. **74**, 5202 (1995)
58 W. Petrich, M.A. Anderson, J.R. Ensher, E.A. Cornell: Phys. Rev. Lett. **74**, 3352 (1995)
59 D.E. Pritchard: Phys. Rev. Lett. **51**, 1336 (1983)
60 Y.V. Gott, M.S. Ioffe, V.G. Tel'kovskii: Nucl. Fusion Suppl. **3**, 1045 (1962)
61 W. Hänsel: Ph.D. thesis, Ludwig-Maximilians-Universität München, 2000
62 J.H. Thywissen, M. Olshanii, G. Zabow, M. Drndić, K.S. Johnson, R.M. Westervelt, M. Prentiss: Eur. Phys. J. D **7**, 361 (1999)
63 D. Cassettari, A. Chenet, R. Folman, A. Haase, B. Hessmo, P. Krüger, T. Maier, S. Schneider, J. Schmiedmayer: Appl. Phys. B **70**, 721 (2000)
64 C. Durkan, M.A. Schneider, M.E. Welland: J. Appl. Phys. **86**, 1280 (1999)
65 M. Drndić, K.S. Johnson, J.H. Thywissen, M. Prentiss, R.M. Westervelt: Appl. Phys. Lett. **72**, 2906 (1998)
66 S. Gov, S. Shtrikman, H. Thomas: J. Appl. Phys. D **87**, 3989 (2000)
67 G. Birkl, F.B.J. Buchkremer, R. Dumke, W. Ertmer: Opt. Commun. **191**, 67 (2001)
68 R. Folman, P. Krüger, J. Schmiedmayer, J. Denschlag, C. Henkel: In *Adv. Opt. Mol. Phys.* (Academic, New York 2002) to appear
69 R. Folman, P. Krüger, D. Cassettari, B. Hessmo, T. Maier, J. Schmiedmayer: Phys. Rev. Lett. **84**, 4749 (2000)
70 D. Müller, E.A. Cornell, M. Prevedelli, P.D.D. Schwindt, Y.-J. Wang, D.Z. Anderson: Phys. Rev. A **63**, 041 602(R) (2001)
71 W. Hänsel, J. Reichel, P. Hommelhoff, T.W. Hänsch: Phys. Rev. Lett. **86**, 608 (2001)
72 Y.B. Ovchinnikov, I. Manek, R. Grimm: Phys. Rev. Lett. **79**, 2225 (1997)
73 T.L. Gustavson, A.P. Chikkatur, A.E. Leanhardt, A. Görlitz, S. Gupta, D.E. Pritchard, W. Ketterle: Phys. Rev. Lett. **88**, 020 401 (2002)
74 E.A. Hinds, C.J. Vale, M.G. Boshier: Phys. Rev. Lett. **86**, 1462 (2001)
75 E. Andersson, T. Calarco, R. Folman, M. Andersson, B. Hessmo, J. Schmiedmayer: Phys. Rev. Lett. **88**, 100 401 (2002)
76 J. Kim, B. Friedrich, D.P. Katz, D. Patterson, J.D. Weinstein, R. DeCarvalho, J.M. Doyle: Phys. Rev. Lett. **78**, 3665 (1997)
77 B. Ghaffari, J. Gerton, W. McAlexander, K. Strecker, D. Homan, R. Hulet: Phys. Rev. A **60**, 3878 (1999)
78 E. Raab, M. Prentiss, A. Cable, S. Chu, D. Pritchard: Phys. Rev. Lett. **59**, 2631 (1987)
79 C. Monroe, W. Swann, H. Robinson, C. Wieman: Phys. Rev. Lett. **65**, 1571 (1990)
80 F. Shimizu, K. Shimizu, H. Takuma: Opt. Lett. **16**, 339 (1991)
81 B. Lounis, J. Reichel, C. Salomon: C. R. Acad. Sci. Paris **316**, 739 (1993)
82 T. Pfau, J. Mlynek: OSA Trends Opt. Photon. **7**, 33 (1997)
83 K.I. Lee, J.A. Kim, H.R. Noh, W. Jhe: Opt. Lett. **21**, 1177 (1996)
84 W. Ketterle, D.S. Durfee, D.M. Stamper-Kurn: In: Proc. Int. Sch. Phys. 'Enrico Fermi', Course CXL, ed. by M. Inguscio, S. Stringari, C. Wieman (IOS, Amsterdam 1999) pp. 67–176
85 M. Greiner, I. Bloch, T.W. Hänsch, T. Esslinger: Phys. Rev. A **63**, 031 401 (2001)
86 E. Mandonnet, A. Minguzzi, R. Dum, I. Carusotto, Y. Castin, J. Dalibard: Eur. Phys. J. D **10**, 9 (2000)
87 B.K. Teo, G. Raithel: Phys. Rev. A **63**, 031 402(R) (2001)
88 Z.T. Lu, K.L. Corwin, M.J. Renn, M.H. Anderson, E.A. Cornell, C.E. Wieman: Phys. Rev. Lett. **77**, 3331 (1996)
89 E. Andersson, M.T. Fontenelle, S. Stenholm: Phys. Rev. A **59**, 3841 (1999)
90 P. Hommelhoff, J. Reichel, W. Hänsel, T.W. Hänsch: to be published
91 F. Treussart, J. Hare, L. Collot, V. Lefèvre, D.S. Weiss, V. Sandoghdar, J.M. Raimond, S. Haroche: Opt. Lett. **19**, 1651 (1994)
92 F. Dalfovo, S. Giorgini, L.P. Pitaevskii, S. Stringari: Rev. Mod. Phys. **71**, 463 (1999)
93 Proc. Int. Sch. Phys. 'Enrico Fermi', Course CXL, ed. by M. Inguscio, S. Stringari, C. Wieman (IOS, Amsterdam 1999)
94 W. Ketterle, N.J. van Druten: In *Advances in Atomic, Molecular and Optical Physics, Vol. 37*, ed. by B. Bederson, H. Walther (Academic, San Diego 1996) pp. 181–236
95 J.T.M. Walraven: In *Quantum Dynamics of Simple Systems*, ed. by G.L. Oppo, S.M. Barnett, E. Riis, M. Wilkinson (IOP, London 1996) p. 315
96 J. Fortagh, H. Ott, A. Grossmann, C. Zimmermann: Appl. Phys. B **70**, 701 (2000)
97 B.P. Anderson, M.A. Kasevich: Phys. Rev. A **63**, 023 404 (2001)
98 J. Fortagh: private communication
99 J.M. McGuirk, G.T. Foster, J.B. Fixler, M.J. Snadden, M.A. Kasevich: Phys. Rev. A **65**, 033 608 (2002)
100 D. Jaksch, H.-J. Briegel, J.I. Cirac, C.W. Gardiner, P. Zoller: Phys. Rev. Lett. **82**, 1975 (1999)
101 Z.O. Garraway, B.M. Garraway: Opt. Commun. **178**, 93 (2000)
102 W. Hänsel, J. Reichel, P. Hommelhoff, T.W. Hänsch: Phys. Rev. A **64**, 063 607 (2001)
103 G. Guthöhrlein, M. Keller, K. Hayasaka, W. Lange, H. Walther: Nature **414**, 49 (2001)
104 J. Ye, D.W. Vernooy, H.J. Kimble: Phys. Rev. Lett. **83**, 4987 (1999)
105 P. Münstermann, F. T., P. Maunz, P.W.H. Pinkse, G. Rempe: Phys. Rev. Lett. **82**, 3791 (1999)
106 N. Schlosser, G. Reymond, I. Protsenko, P. Grangier: Nature **411**, 1024 (2001)
107 H. Mabuchi, M. Armen, B. Lev, M. Loncar, J. Vuckovic, H.J. Kimble, J. Preskill, M. Moukes, A. Scherer: Quant. Inf. Comp. **1**, 7 (2001)
108 Y. Sortais, S. Bize, M. Abgrall, S. Zhang, C. Nicolas, C. Mandache, R. Lemonde, P. Laurent, G. Santarelli, N. Dimarcq, P. Petit, A. Clairon, A. Mann, A. Luiten, S. Chang, C. Salomon: Physica Scripta **T95**, 50 (2001)